Supplementary Materials for

Inhibitors of bacterial H_2S biogenesis targeting antibiotic resistance and tolerance

Konstantin Shatalin†, Ashok Nuthanakanti†, Abhishek Kaushik, Dmitry Shishov, Alla Peselis, Ilya Shamovsky, Bibhusita Pani, Mirna Lechpammer, Nikita Vasilyev, Elena Shatalina, Dmitri Rebatchouk, Alexander Mironov, Peter Fedichev, Alexander Serganov, Evgeny Nudler*

†These authors contributed equally to this work.
*Corresponding author. Email: evgeny.nudler@nyulangone.org

Published 11 June 2021, *Science* **372**, 1169 (2021)
DOI: 10.1126/science.abd8377

This PDF file includes:

Other Supplementary Materials for this manuscript includes the following:
(available at science.sciencemag.org/content/372/6547/1169/suppl/DC1)

MDAR Reproducibility Checklist (.pdf)
Movies S1 to S4 (.mp4 and .mov)

Materials and Methods

Strains and growth conditions

S. aureus and *P. aeruginosa* strains were grown in Trypticase Soy Broth (TSB) or Lysogeny broth (LB) without or with 200-400 μM L-cysteine and on LBA plates (LB supplemented with 1.5% Bacto agar) at 37 °C.

Wild-type *S. aureus* USA300 isolate JE2 (MRSA) as well as its *cbs/cse* and *cse* mutants were obtained from the Nebraska Knockout collection; Newman strain was obtained from Dr. Torres (NYU School of Medicine), RN4220 strain and bacteriophage 80γ from Dr. Novick (NYU School of Medicine), and RN10659-RN10667 hospital vancomycin resistant strains were obtained from Dr. Shopsin (NYU School of Medicine). *cbs* and *cse* deletions without causing polarity were constructed in *S. aureus* RN4220 strain according to a method described previously (*66, 67*) **(Table S1).** Briefly, Km cassette in the pKS1 was flanked with 0.5 and 0.7 kb fragments, which were amplified from bacterial genomic DNA by using oligonucleotides:
GGGGCGGCCGCTTAGAATTAAATGTTTCTAACTTCAC;
GGGCTGCAGCATAGATGCACCCTCATCTGAC;
GGGGTCGACGAAAACTAAATTAATTCACGGTGG;
GGGCTCGAGCAGCAACGACATCACTATGTCC;
GGGGCGGCCGCACTGCTGGTAATACAGGCATAG;
GGGCTGCAGCATTCTCCTCATAATTAAATATTTGC;
GGGAAGCTTGTTATAAATAATAGCAGCACTGGC;
GGGCTCGAGATTGAAATGCTGAAATATCATACCG. Then these recombinant plasmids were used for *cbs* and *cse* gene replacement. Mutations from RN4220 and MRSA were transduced to other *S. aureus* strains by bacteriophage 80γ (*68*). For complementation, the same recombinant plasmid carrying *cse* instead of Km cassette was transformed in the *cse* deletion mutant followed by the integration into chromosome.

Wild-type *P. aeruginosa* strain PA01 and its Tn-based *cbs/cse* and *cse* mutants were obtained from University of Washington Genome Sciences mutant collection; and PA14 wt, *cbs/cse* and *cse* Tn-based mutants were obtained from Massachusetts General Hospital Transposon Mutant Library. A *cbs/cse* deletion in PA01 was obtained from Dr. Yongzhen Xia (Shandong University, China). Complementation in *P. aeruginosa* was done according to ref. (*69*). The *cse* gene was amplified by PCR with primers:
F_PA01cse GGGGAATTC**A**TGAGCCAGCACGACCAGC and
R_PA01cse GGGAAGCTTCAGATCTTCGCCAGCGCCTG from gDNA and the PCR product was purified and digested with *Eco*RI and *Hind*III. The digested PCR product was then ligated into *Eco*I/*Hind*III-treated pUCP24 to generate pUCP-*cse*. The *Δcbs/cse* complementation strain was generated by electroporation of pUCP-*cse* into PA01 *Δcbs/cse* followed by selection on LB agar containing gentamicin (200 μg/ml)

P. aeruginosa has a single amino acid difference in *cbs* (T78A) and in *cse* (Y32F) between the PAO1 and PA14 strains. RNA4220, USA300, and Newman strains of *S. aureus* have identical *cbs*/*cse* nucleotide sequences.

Chemicals

All chemicals, unless specified otherwise, were purchased from Sigma. WSP5 was provided by Dr. Xian (*70*). NL1, NL2, NL3, NLF_3, and TICT-based fluorescent H_2S probe (*28*) were custom synthesized by Enamine Ltd. NL1 was also supplied by InterBioScreen Ltd (NJ, USA).

Generation of growth curves

Growth curves were obtained on a Bioscreen C automated growth analysis system (BioTek Instruments Inc.). Subcultures of specified strains were grown overnight at 30 °C, diluted in fresh media 1:500, and grown with aeration until 1×10^8 cell/ml at 37 °C. The cultures were diluted 1:100 in LB or LB supplemented with L-cysteine media and mixed with the equal volume of an antibiotic and/or reagent dissolved in the same media, as described in the text or figure legends. 200 µl of each mixture with 5×10^5 bacteria/ml was inoculated into the honeycomb wells in triplicate and grown at 37 °C with maximum shaking on the platform of the Bioscreen C instrument. OD_{600} values were recorded automatically at different time points and the means of triplicates plotted.

H_2S detection

Lead acetate detection method (*71*) was used to measure gaseous H_2S exiting solution. Paper strips saturated by 2% of Pb-acetate were affixed to the inner wall of a cultural tube, above the level of the liquid culture of wild type or mutant bacteria. Overnight cultures were diluted 1:50 in LB without or with L-cysteine for *S. aureus* (200 – 500 µM) and TSB for *P. aeruginosa* and incubated at 37 °C with aeration for 12-20 h. Stained paper strips were scanned and quantified with an AlphaImager™ system (Alpha Innotech).

MBB fluorescence detection probe (*27*) was used to measure gaseous H_2S exiting solution. Overnight cultures were diluted 1:20 in LB with 0.8 mM L-cysteine. 200 µL aliquots per well were transferred to the 96-wells plate. Nitrocellulose membrane soaked with MBB solution (100 mM Tris-HCl, pH 8.8, with 184 µM MBB) was used to tightly cover the wells above the level of the liquid culture. Plates were then covered with lid, sealed with parafilm M, and incubated for 16 hours at 37 °C with shaking using Cytation 3 instrument (BioTek Instruments Inc.). The membrane fluorescence was then analyzed using FluorChem R (ProteinSimple, USA).

Fluorescent-based detection methods were used to measure H_2S dissolved in solution. TICT-based fluorescent H_2S probe (3 µM) was added to liquid bacterial culture. After 40 min, the aliquots were taken for fluorescent microscopy using API DeltaVision PersonalDV system with Olympus IX-71 inverted microscope base. Images were taken with an Olympus PlanApo N 60×/1.42 oil lens. WSP5 fluorescent H_2S probe (*70*) was used for quantitative H_2S detection in bacterial cultures and biochemical (IC_{50}) assays using Cytation 3 instrument (BioTek Instruments Inc.). The values obtained with bacteria were normalized to ODs of the cultures. The concentrations of H_2S were determined from a standard curve obtained with NaHS, which is a source of H_2S. Concentrations of NL1-3 used in Fig. 2B experiments were 32 µM for *S. aureus* and 180 µM for *P. aeruginosa*.

Pyocyanin quantitation

Cells from overnight cultures were precipitated by centrifugation and supernatant was collected and filtered. Pyocyanin was extracted by chloroform. Samples were centrifuged for 10 min at 10,000 rpm and chloroform/pyocyanin mixture was transferred to a new tube. Pyocyanin was extracted from the mixture by 0.2 N HCl and was collected as pink–red solution by centrifugation for 2 min at 10,000 rpm. Quantification of the pyocyanin in the solution was carried out by measuring absorbance at 520 nm (*72*).

Protein preparation

Full-length wild-type *Staphylococcus aureus* cystathionine-γ-lyase (SaCSE) was overproduced with N-terminal decahistidine and SUMO tags using T7 RNA polymerase-based expression system and *E. coli* BL21(DE3) strain. Expression of the SaCSE gene was induced by the addition of 0.2 mM isopropyl β-D1-thiogalactopyranoside (IPTG) and the culture was grown for 5 hours at 37 °C. Cells were collected by centrifugation and resuspended in the lysis buffer that contained 20 mM Tris–HCl, pH 8.0, 0.5 M NaCl, 5 mM imidazole, 5 mM β-mercaptoethanol (BME) and EDTA-free protease inhibitor (Roche). Cells were lysed by sonication and the protein lysate was clarified by centrifugation. Supernatant was loaded onto a 5 ml HisTrap FF column (GE Healthcare), the column was washed with the lysis buffer, and the protein was eluted with the lysis buffer supplemented with 0.25 M imidazole. Fractions containing the protein were combined and the His_{10}-SUMO tag was removed by the His_6-tagged ULP1 protease at 4 °C for 14–16 h. This cleavage left a serine instead of the initiatory methionine at the N-terminus of the protein. The digestion products were dialyzed against the lysis buffer without imidazole (20 mM Tris–HCl, pH 8.0, 0.05 M NaCl, 5 mM BME), and the His_6-tagged ULP1 and His_{10}-SUMO tag were removed by the affinity chromatography on a HisTrap FF column. The flow-through that contained SaCSE was concentrated and purified by ion-exchange chromatography on Hi-Prep Q Sepharose Fast Flow 16/10 (GE Healthcare). The protein sample was loaded onto the column equilibrated with 20 mM Tris–HCl, pH 8.0, 50 mM NaCl, and 5 mM BME, and the protein was eluted with a gradient of the same buffer supplemented with 1.0 M NaCl. Fractions containing SaCSE were combined and dialyzed against 20 mM Tris–HCl, pH 8.0, 0.1 M NaCl, 5 mM BME overnight. Finally, SaCSE was purified by gel filtration on Superdex 200 (GE Healthcare) in 20 mM Tris–HCl, pH 8.0, 0.1 M NaCl, and 5 mM BME and stored at 4 °C for immediate use. For long-term storage, small aliquots of the protein were flash-frozen in liquid nitrogen and stored at −80 °C. The SaCSE variants containing Y103N, Y103A and H339A mutations were prepared in the same way as the wild type protein. *Pseudomonas aeruginosa* CSE (PaCSE) was prepared by the procedure similar to the purification of the wild-type SaCSE except that the ion-exchange chromatography step was omitted. Human cystathionine-γ-lyase (hCSE) was prepared as in ref. (*30*).

IC_{50} assay

Florescence spectrophotometry-based inhibitory activity towards purified CSE enzymes was measured using the Corning plate (catalog #3651) in 100 μL of the reaction mixture per well. bCSEs and hCSE (0.1 μM) in 50 mM Na-phosphate buffer, pH 8.0, supplemented with 10 μM PLP and 1.2 or 2.0 μM WSP5 (excitation: 500 nm, emission: 530 nm) were preincubated for 20 min with different concentrations of the inhibitor under test. The reaction was initiated by adding 100 μM (or 2.2 mM in selected cases) L-cysteine to the reaction mixture and the enzymatic activity was monitored using the Cytation 3 instrument (BioTek Inc.). Note that the 100 μM L-cysteine concentration used in the experiments corresponds to the maximal intracellular concentration reported in bacterial cells (*43*). The data were fit by non-linear regression to the Dose-response - Inhibition model; [Inhibitor] vs. response (three parameters), in GraphPad Prism 7 software. Each experiment was conducted with 2-3 technical replicates. IC_{50} values were mean of 2-6 independent experiments.

Microscale thermophoresis

SaCSE was labeled using the RED-NHS fluorescent dye according to the labeling protocol of the manufacturer (NanoTemper Technologies). A series of dilutions of NL1 and $NL1F_3$ were prepared using a buffer solution containing 50 mM Tris-HCl, pH 7.5, 1 mM CHAPS, and 10% DMSO. The

enzyme solution was prepared with the same buffer but without DMSO. The labeled SaCSE was mixed at 1-to-1 ratio with different amounts of compounds yielding a final concentration of 50 nM of the fluorescently labeled protein, and the final inhibitor concentrations in the range indicated in the figure panels. Samples were incubated at room temperature for 10 min and then loaded onto Monolith NT Premium Capillaries (NanoTemper Technologies). The thermophoresis was conducted on a Monolith NT.115 instrument at LED power of 20-30% and MST power of 60%. The K_D was determined by nonlinear fitting of the thermophoresis responses from three independent experiments using GraphPad Prism 6 software.

Estimation of molecular weight by gel-filtration chromatography

Gel-filtration chromatography of wt and mutated CSEs was performed on Superdex 200 10/300 GL column (GE Healthcare) in 20 mM Tris–HCl, pH 8.0, 0.2 M NaCl, and 1 mM DTT, in the absence or presence of 0.250 mM PLP. Injection volumes were 0.4 mL with 1 mg/mL (0.025 mM) protein concentration. The molecular weight standards used for calculating the standard curve were carbonic anhydrase (29 kDa), ovalbumin (44 kDa), conalbumin (75 kDa), and aldolase (158 kDa). The graph used for estimation of the molecular weights of CSEs was prepared by plotting Log(Mr) against Kav, where Kav=Ve-Vo/Vc-Vo. Vc, Vo and Ve are column, void and elution volumes, respectively.

Antibiotic MIC and MBC determination

Standardized minimum inhibitory concentrations (MICs) were determined by the modified broth microdilution method specified by the Clinical and Laboratory Standards Institute (CLSI) (*73*). Briefly, the test antibiotic was serially diluted twofold in 100 µl LB (for *S. aureus*) or TSB (for *P. aeruginosa*) with or without the indicated amounts of bCSE inhibitors. The bacteria inoculum was 100 µl of a 1.0×10^6 CFU/ml dilution in LB or TSB supplemented with 200 µM L-cysteine. The MIC was the lowest concentration of antibiotic that prevented turbidity after 24 h of incubation at 37 °C. The minimum bactericidal concentrations (MBCs) were defined as the lowest concentration of antibiotic that generated <1% survival of the initial inoculum. Briefly, the MBC was determined by transferring 100 µl from each tube containing no visible bacterial pellet and plating on TSB agar after serial dilutions. The plates were incubated at 37 °C for 24 h prior to colony counting. When 99.9% of the bacterial population is killed at the lowest concentration of an antibiotic, it is defined as MBC endpoint. This was achieved by observing pre- and post-incubated agar plates for the presence or absence of CFUs.

Persister assay (time-dependent killing)

Overnight bacterial cultures were diluted 1:1,000 in LB and continued growing on a shaker (250 rpm) at 37 °C for 3 h to reach the exponential phase. Aliquots of cells in 15 ml Falcon culture tubes were challenged by adding an appropriate antibiotic with or without the exogenous slow-releasing H_2S donor [0.25% garlic oil blend from Sigma, corresponding to 1.4 mM diallyl trisulfide (*74*)] and incubated on a shaker at 37 °C for 3 h. At the designated time points, a sample was removed, diluted, and 10 µl aliquot was spotted on an antibiotic-free LB agar plate for counting colony-forming units (CFU) (*75*).

Colony morphology assay

P. aeruginosa strains were grown in LB medium to the late exponential phase. 10 µl aliquots were spotted onto 1% agar plates containing 10 g/L Tryptone Broth, supplemented with 40 µg/L Congo

Red and 20 μg/L Coomassie Blue, as described previously (*58*). Plates were incubated at 22 °C for 3 days with or without NL1 (180 μM).

Biofilm assay

Solid surface associated biofilm quantification assay was performed in microtiter plates using crystal violet staining according to published protocols (*76, 77*). Briefly, overnight cultures were diluted to 1 ~ 2 × 10^6 CFU/ml in TSB supplemented with 0.2% glucose. 200 μL aliquots were distributed to each well of a flat 96-well microtiter plate (Corning) and incubated at 37 °C for 24 h. Planktonic cells were removed and wells were washed with phosphate-buffered saline (PBS). 200 μL crystal violet solution (0.1%, v/v) was added to each well and incubated at 37 °C for 15 min. NL1-3 (64 μM for *S. aureus* and 180 μM for *P. aeruginosa*) were added 24 h prior to removing planktonic cells and staining with crystal violet. Crystal violet solution was removed and wells were washed with PBS 4 times. 200 μL of glacial acid (30%, v/v) was added to each well and absorbance was measured at 595 nm using a BioTek Cytation 3 instrument.

Structure-based virtual screening

We utilized the crystal structure of the SaCSE holoenzyme for the search of druggable binding sites. All inorganic ions and water molecules were removed. The PLP-bound Lys196 was converted into unmodified lysine residue. The hydrogen and charges were added using Chimera plugin DockPrep with default settings (*78*). Assignment of charges was done using AMBER ff14SB for standard residues and AM1-BCC for other residues. *In silico* prediction of drug-binding areas using cavity detection server PockDrug (*79*) with Fpocket (*80, 81*) pocket estimation method. The ligand proximity threshold was 5.5 Å.

The centroid-based virtual screening was performed in several steps. The combined library of 3,224,758 compounds, available from commercial suppliers Alinda, Asinex, ChemDiv, Enamine and InterBioScreen, was clustered using the Jarvis–Patrick algorithm (*82-84*). The measure of dissimilarity ("distance") between the molecules was determined by Tanimoto similarity calculated with Daylight fingerprints of the molecules (Daylight Chemical Information Systems, Inc.; Aliso Viejo, CA). The clustering parameters were chosen to obtain a reasonable number of clusters (73,560). As a result, the combined compound library was reduced to a library of roughly 73,000 cluster representatives of appropriate molecular weight. The compounds were prepared for docking by extraction from the commercial provider-supplied sdf files, generation of the protonation states and three-dimensional structures with the help of OpenBabel package v.2.3.1 (*85*) in batch mode.

Docking was conducted by AutoDock Vina 1.1.2 with default parameters (*41*). The compounds representing cluster centroids were used with a docking box of 17.25 × 19.50 × 26.25 Å and center at [28.97, 52.10, -22.72]. The resulting docked structures were ranked according to their predicted binding energy. 113,828 compounds similar to the top-ranking centroids were searched in the library and screened with the same parameters two times. 44 top hits from all docking procedures were selected for biology testing.

Crystallization

Crystallization trials with SaCSE were performed by the vapor diffusion method in the 96-well sitting drop plates using commercial sparse matrix kits (Qiagen and Hampton Research) and Mosquito crystallization robot at 18 °C. The protein was at 0.15 mM concentration in a solution of 20 mM Tris–HCl, pH 8.0, 0.1 M NaCl, and 1 mM BME. Initial crystallization conditions were

identified in the Classic Suite screen (#44 from Qiagen): 0.1 M HEPES-Na, pH 7.5, 1.4 M trisodium citrate. Larger crystals of SaCSE were grown by hanging drop vapor diffusion from a solution prepared by mixing 1.5 µl of 0.15 mM SaCSE and 1.5 µl of reservoir solution comprised of 0.1 M Tris–HCl, pH 7.6, and 1.4 M trisodium citrate. The drops were equilibrated against 1 mL of the reservoir solution at 18 °C for 3–7 days until crystals reached 0.1 × 0.2 × 0.2 mm size. The protein was co-purified partially with the bound co-enzyme pyridoxal phosphate (PLP) and was crystallized in the state prior to the PLP conjugation with Lys196.

To form the holoenzyme, SaCSE solution was supplemented by 1.5 mM PLP. All other crystals reported in our study were obtained by the same protocol by slightly varying the concentration of trisodium citrate and changing the buffer (Tris–HCl, HEPES-Na, or Na-cacodylate). Specifically, the SaCSE holoenzyme crystals containing HEPES-Na were grown using reservoir solution with 0.1 M HEPES-Na, pH 7.5, and 1.3 M trisodium citrate. Identical conditions were used to obtain holoenzyme structures of the SaCSE mutants. Crystals of the holoenzyme dimer were obtained by using the reservoir solution composed of 0.1 M Tris–HCl, pH 7.6, and 1.2 M trisodium citrate. To prepare AOAA-bound crystals, aminooxyacetic acid (AOAA) was soaked into the holoenzyme dimer crystal by adding 0.4 µl of solution containing 10 mM AOAA, 0.1 M Tris–HCl, pH 7.6, and 1.2 M trisodium citrate to the drop and incubating for 2 hours prior to picking up the crystals. The holoenzyme structures for both wild type and mutants in the presence of the lead H_2S inhibitors were obtained from the crystals grown in the hanging drops prepared by mixing 1.5 µl of the protein solution and 1.5 µl of the reservoir solution. The protein solution contained 0.15 mM SaCSE, 1.5 mM PLP, 3 mM lead compound, 20 mM Tris–HCl, pH 8.0, 0.1 M NaCl, and 1 mM BME. The reservoir solutions were 0.1 M Tris–HCl, pH 7.6, 1.2 M trisodium citrate for NL1 and wt SaCSE and the Y103N mutant; 0.1 M Tris–HCl, pH 7.6, and 1.3 M trisodium citrate for NL2 with wt SaCSE; 0.1 M Tris–HCl, pH 7.6, and 1.4 M trisodium citrate for wt SaCSE with NL3; 0.1 M HEPES, pH 7.6, and 1.4 M trisodium citrate for wt SaCSE with $NL1F_3$; 0.1 M HEPES, pH 7.6, and 1.2 M trisodium citrate for NL2 and the Y103N mutant; 0.1 M HEPES-Na, pH 7.5, 1.3 M trisodium citrate for NL1 and the Y103A mutant; Na-cacodyate, pH 6.5, 1.3 M trisodium citrate for NL2 and the Y103A mutant. Crystals were cryoprotected by immersing into reservoir solution supplemented by 20% (v/v) glycerol and flash-frozen in liquid nitrogen.

Data collection, structure determination and analysis

Diffraction data were collected at the beamlines FMX and AMX of the National Synchrotron Light Source-II (Brookhaven National Laboratory) and beamlines 24-ID-C and 24-ID-E of the Advanced Photon Source (Argonne National Laboratory) at 100 K. Data were processed by XDS suite (*86*) or HKL2000 (HKL Research). The initial crystal structure of wt SaCSE in $I4_122$ space group was solved by molecular replacement using the structure of the CSE-like enzyme from *Xanthomonas oryzae* (PDB ID code: 4IXZ) (*39*) and PHASER in PHENIX (*87*). All other structures were determined based on this initial structure. The structural models of the protein were improved by iterative cycles of manual building in Coot (*88*) and refined in PHENIX. Drug molecules and components of crystallization solution were added at the final stage of refinement based on the $F_O–F_C$ and $2F_O–F_C$ electron density maps, and diagnostic anomalous signal of Br atoms. The structures were adjusted when necessary based on the $2F_O–F_C$ simulated annealing composite omit maps. Details of small molecules modelling are outlined below. Statistics of diffraction data processing and the model refinement are given in Tables S4–S6. Cavity volume

was calculated by MOL2 (*89*). Intermolecular interfaces and buried surface areas were calculated by PISA (*90*).

Structure building

Wt SaCSE with bound PLP. SaCSE is a homotetramer with the catalytic site involving amino acids from two protomers. The protein has high affinity to PLP and is co-purified with PLP. Crystallization of the protein retains PLP bound in the catalytic site; however, Y99, a key amino acid that stacks on the ring system of PLP and facilitates conjugation with K196, is rotated outwards. Therefore, bound PLP does not link with K196, as demonstrated by the lack of the electron density map connecting PLP and K196. In addition, the density map for the ring system shows that PLP is inclined towards the position occupied by Y99 in the holoenzyme. Therefore, PLP was modelled as a stand-alone molecule at the occupancy lower than 100% and in a conformation distinct from the PLP conjugated with K196.

Wt SaCSE holoenzyme. We found that adding excess of PLP (1.5 mM) to the SaCSE sample drives conformational rearrangement of Y99 that in turn causes conjugation of PLP with K196, as revealed by the excellent density map connecting these two moieties. In addition, we found an extra map connected to the N-terminus of the enzyme, and modeled it as the Ser1-linked PLP. This serine substitutes the initiatory methionine of the protein, which is cleaved off in the natural protein. Therefore, PLP-Ser1 conjugation is an artifact of crystallization. The site with the N-terminally bound PLP corresponds to Site 2 of the lead-bound structures.

Wt SaCSE dimer and AOAA soaked structures. Slightly lower salt concentration during crystallization could lead to a different crystal form with $P4_322$ space group and two protein molecules in the asymmetric unit. Although the structures in $P4_322$ and $I4_122$ space groups are similar, only $P4_322$ crystals were compatible with AOAA binding during soaking. AOAA has excellent map connecting it with PLP while the map for the PLP-K196 connection is lacking. The two AOAA molecules present in the asymmetric unit have slightly different conformations of flexible moieties.

Wt SaCSE bound to NL1. The major lead-binding site (Site 1) of SaCSE is predominantly composed of amino acids of a single protomer. However, a symmetry related CSE molecule blocks the entrance to the pocket and the lead H_2S inhibitors soaked into the holoenzyme crystals have difficulty entering the pocket. Therefore, all structures with the inhibitors were obtained by crystallization of the protein-lead complexes preformed in solution. The crystallographic data for the NL1-bound structure was of exceptional quality that allowed detecting anomalous signal at over 5 σ level for sulfur atoms in several methionines. Consecutively, the anomalous signal of the bromine atom of NL1 reached 20 σ level in Site 1 and, together with excellent omit maps, allowed unambiguous modelling of the lead and refinement with high 72% occupancy. The positive $2F_O–F_C$ map at the Br atom indicates that the actual occupancy of the lead is higher. However, the tail of the lead is more dynamic, as exemplified by positive $2F_O–F_C$ map peaks along this moiety, and likely decreases the overall occupancy. Aside of methionines, the high sensitivity of anomalous maps allowed detecting anomalous signal at >5 σ level in four more sites. The anomalous peaks coincided with $2F_O–F_C$ maps and were treated as minor sites of NL1 binding. However, both refined and unbiased density maps did not have sufficient uninterrupted density for modelling of the entire NL1, indicative of very low occupancy and conformational heterogeneity of the bound lead. Therefore, we modelled only the Br atom of NL1 and assigned remaining density peaks to water molecules in Sites 3−5. Site 2 contained both anomalous signal (12.8 σ) and the $2F_O–F_C$ map for connecting PLP with Ser1, suggesting the presence of both molecules in the same site.

The shape of the omit maps suggested a mixture of two molecules, therefore, we modelled both Ser1-conjugated PLP and NL1 in the same site and refined occupancy in Phenix. The final occupancy was 33% for NL1 and 39% for PLP. Thus, Site 2 is a non-specific site capable of binding to various planar molecules. As mentioned above, Site 2 does not exist in the natural SaCSE.

Y103N mutant bound to NL1. The Y103N mutation significantly decreased occupancy of NL1 in Site 1 as shown by the anomalous peak level (6.6 σ) lower than the levels in practically all minor binding sites. Nevertheless, two separate pieces of the density map partially corresponding to both indole and tail of the lead allowed modelling of entire NL1 in Site 1 and refining it to 29% occupancy. Site 2 did not have good density map and lacked the density for the Ser1-PLP connection. We modelled only NL1 and refined it to 47% occupancy in this site. Site 3 had two large pieces of unbiased map for indole and tail that let us model the entire NL1 and refine it to 51% occupancy. Sites 4 and 5 had very little density map sufficient to place only Br atoms. Reduction in NL1 binding in Site 1 caused reciprocal appearance of two new minor sites, Sites 6 and 7, with the density map sufficient to model the indole moiety of the lead and refine it to 52% and 47%, respectively.

Y103A mutant bound to NL1. The absence of anomalous signal indicated the absence of NL1 in Site 1. Therefore, small peaks of density map present in the site were modelled as water molecules. In Site 2, NL1 was modelled without PLP based on the same observations as in the Y103N mutant. Site 3 had sufficient density to model only Br atom of the lead.

Wt SaCSE bound to NL2. Given more constrained conformation of NL2, the lead bound to the protein only in Site 1, where it was refined to 77% occupancy.

Y103N mutant bound to NL2. There was no anomalous signal above background in any of the lead-binding sites. In site 1, the density map peaks were modelled as molecules of the solvent.

Y103A mutant bound to NL2. This mutant provided more space in Site 1 and we detected two anomalous signals, suggesting two alternative binding modes of NL2. Although the $2F_O–F_C$ omit density map was of low quality, two flat pieces of the density map suggested alternative placement of the NL2 moieties so that the tail of one molecule shares space with the indole of the second NL2. None of these conformations, refined to 26 % and 40% occupancy, matched the conformation of NL2 bound to wt SaCSE. While in one conformation the indole was placed in a similar way in the pocket, the furan moiety fitted the density map better in the flipped conformation.

Wt SaCSE bound to NL3. NL3 has lower aqueous solubility than NL1 and NL2 and its electron density map was less well-defined. To model NL3, we compared unbiased $2F_O–F_C$ simulated annealing composite omit maps calculated from different crystals with NL3. The final model was refined against data from a single crystal to 64% occupancy.

Quantitative proteomics

Preparation of mass spectrometry samples

Bacterial pellets were resuspended in the lysis buffer containing 100 mM NH_4HCO_3, 10 mM DTT and 1% SDS. Samples were heated at 95 °C for 10 min and then cooled at room temperature. Samples were mixed with 1/10 vol. of freshly prepared 0.5 M iodoacetamide followed by 30-min incubation at room temperature in dark. After alkylation, proteins were precipitated with 4 vol. of acetone at -20 °C for 1 h and then re-dissolved in the solution of 50 mM NH_4HCO_3 and 8 M urea.

For digestion, protein samples were diluted ten-fold with the solution containing 50 mM NH_4HCO_3 and 10-20 ng/µl trypsin (Sigma) followed by overnight incubation at 25 °C. Trypsin-

to-protein mass ratio was kept around 1:20. Resulting peptides were desalted using C18 spin tips (Pierce) according to manufacturer protocol, dried under vacuum, and re-dissolved in 0.1% formic acid.

LC-MS analysis of peptides

Peptides were analyzed in the Orbitrap Fusion Lumos mass spectrometer (Thermo Scientific) coupled to Dionex UltiMate 3000 (Thermo Scientific) liquid chromatography system. Peptides were resolved on 50-cm long EASY-Spray PepMap RSLC C18 column using 90-min linear gradient from 96% buffer A (0.1% formic acid in water) to 40% buffer B (0.1% formic acid in acetonitrile), followed by 96% buffer B over 5 min with a flow rate of 250 nl/min. Data-dependent acquisition protocol was based on published CHOPIN method (*91*) except the duration of each cycle was reduced from 3 to 2 s.

Data processing and analysis

Raw data were processed using MaxQuant (*92*). List of protein sequences included whole proteomes of *Staphylococcus aureus* (strain NCTC 8325 / PS 47) or *Pseudomonas aeruginosa* (strain UCBPP-PA14) downloaded from Uniprot database (https://www.uniprot.org) concatenated with list of known protein contaminants. Label-free quantitation and match between runs options were enabled whereas other parameters in MaxQuant were left unchanged. Statistical analysis was done in R computing environment.

Cytotoxicity assay

BJ-5ta (cat. ATCC CRL-4001, American Type Culture Collection, USA), were cultured in MEM medium (cat. 11095-080, Invitrogen) containing 10% heat inactivated fetal bovine serum (Invitrogen), non-essential amino acids, 100 IU penicillin and 100 μg/ml streptomycin (Invitrogen). Cells were maintained at 37 °C with 5% CO_2. The assay was conducted for 22 h using a multiplex labeling with IncuCyte NucLight BacMam 3.0 reagent (cat. 4621, Essen Bioscience) for nuclear labeling of live cells and the Cytotox Green reagent (cat. 4633) to detect dead cells. Cells were harvested and resuspended at 2×10^4 cells/mL in growth medium. The Red NucLight BacMam 3.0 Reagent and the Cytotox Green reagents were 1% (v/v) solutions. Cells were seeded at 2×10^4 and the images were captured and analyzed using IncuCyte ZOOM Live-Cell Analysis System (Essen BioScience) with and a 4× objective lens. The light sources were an argon laser and white light laser. The excitation wavelengths were 488 nm and 591 nm. The emission wavelengths were 500–540 nm for SSP4 (PMT; Gain: 1000) and 600–650 nm for RFP (HyD; Gain: 100).

Trypan blue exclusion assay

Human Brain Microvascular Endothelial Cells (HBMEC) were purchased from Cell Systems. The cells were cultured in Complete Classic Medium (Cell Systems) supplemented with 10% serum and activated with CultureBoost (Cell Systems) and Bac-Off antibiotics reagent (4Z0-644, Cell Systems), which contains 2.4 mg/ml of ciprofloxacin. HBMEC were pre-treated with NL1 as indicated in the **Fig. S10**. Cells were recovered for 24 h. Cell viability was calculated by counting the unstained live cells and the blue-stained dead cells with a hemocytometer.

CellTiter-Glo assay

The experiments were conducted with the following cell lines: Normal Human Dermal Fibroblast -Neonatal (NHDF) from Lonza, NHDF- Adult from Lonza, Human dermal Fibroblast (HDFa) from ATCC, and Normal human lung fibroblast MRC9 from ATCC. 5,000 cells per well were

plated in a 96 well plate overnight. Cells were treated with NL1 alone or with NL1 plus gentamicin for 24 h. Cell vitality was determined as their ability to produce ATP using an ATP luminescent cell viability assay (CellTiter-Glo kit, Promega, cat. G7570). 100 µl of the CellTiter-Glo reagent was added to the cell culture medium in each well and mixed for 2 min on an orbital shaker to induce cell lysis. The plate was incubated at room temperature for 10 min. Luminescence was measured using Cytation3 system.

Apoptosis assay

HBMEC were treated with 200 µM NL1 for 6 h. The cells were stained with the APC Annexin V Apoptosis Detection Kit with PI (BioLegend). The cells were washed twice with the Cell Staining Buffer (BioLegend) and resuspended in the Annexin V Binding Buffer. 100 µL of the cell suspension was transferred to 5 mL flow cytometry tubes and incubated with 5 µL Annexin V and 10 µL PI in the dark at room temperature for 15 min. Cells were strained and kept on ice prior to flow cytometry. Data analysis was performed using FlowJo Version 10.7.0 (BD Biosciences).

Murine lung infection model

The study was performed at the facilities of VibioSphen, Prologue Biotech, Labège, France. All procedures were performed according to the approved written study protocol and standard operating procedures (SOPs), and in accordance with the Directive 2010/63/UE recommendations and the French Veterinary Authorities agreement. All procedures performed on animals were approved by the Institutional Animal Care and Use Committee (IACUC). The *in vivo* protocol design and procedures were approved by the Ethical Committee under ethical protocol #CEEA-122 2014-53.

5-6-week-old female Swiss mice (RjOrl:SWISS:CD-1®, 22-25 g) were obtained from Janvier Labs (St. Berthevin, France,) and acclimated in the animal facility for 4 days. *P. aeruginosa* PA14 vial was thawed and cultured for 24 h. 2 ml of this preculture were diluted in 98 ml TSB. After 2 h of growth, at OD_{600} of 1.68, bacteria were collected and diluted in PBS to obtain the appropriate quantity per mouse. Mice were flash anesthetized with isoflurane gas and infected intranasally with 1.3×10^6 CFU/mouse of bacteria in 50 µl. At 30 min after infection, gentamicin and NL1 were administered by subcutaneous (s.c.) route at 10 ml/kg. Group 1: Vehicle 1 + vehicle 2 (n=16); Group 2: Gentamicin (2 mg/kg) + vehicle 1 (n=16); Group 3: Gentamicin (2 mg/kg) + NL1 (60 mg/kg) (n=10); Group 6: NL1 (60 mg/kg) + vehicle 2 (n=10). Vehicle 1 was 0.9 % NaCl and vehicle 2 was PBS supplemented with 10% DMSO. 5 h after infection, mice were sacrificed to collect lungs. Lung tissues were weighted and homogenized in Precellys beads tubes. The resultant homogenate was serially diluted. The dilutions were spotted onto TSA plates and grown overnight at 37 °C. CFU were quantified for each dilution. Bacterial burdens were calculated per lung for each mouse and per group of animals. In designing this experiment, we followed the reasoning of (*93*) (and examples therein) with respect to murine models of acute pneumonia; and generally followed the examples of (*94, 95*), albeit providing some extra time (30 min) between the inoculation and the administration of the treatments.

Murine sepsis model

The study was performed at the facilities of TransPharm Preclinical Solutions (The Wellhoff Center, Jackson, MI, USA). Female Swiss Webster mice (Envigo, ND4; Model code 032, 19-21 g), were acclimated to housing conditions and handled in accordance with AUP number TP-01. Animals were acclimated for at least 24 h prior to the start of the experiment. The animals were

fed the irradiated Teklad Global Rodent Diet and water *ad libitum.* Mice were housed 5/cage in static cages with the irradiated Teklad 1/8" corn cob bedding inside bioBubble Clean Rooms that provide H.E.P.A filtered air into the bubble environment at 100 complete air changes per hour. Treatment groups were identified by cage card. All procedures carried out in this experiment were conducted in compliance with the laws, regulations, and guidelines of the National Institutes of Health and with the approval of the TransPharm Animal Care and Use Committee.

S. aureus Newman was grown in 5 mL of TSB at 37 °C in ambient atmosphere overnight. The culture was diluted 1:100 in 5 mL of TSB and grown at 37 °C for 3 h. The culture was then centrifuged at 4,000 rpm at 4 °C for 5 min. The pellet was re-suspended in 5 mL of PBS, centrifuged a second time, and resuspended in 5 mL of PBS. Assuming an OD_{600} of 1.0 = 10^9 CFU/mL, the culture was diluted to provide a challenge inoculate, back-counted at 2.5×10^7 CFU per mouse, via intravenous injection with a volume of 0.1 mL of PBS. Instillation of the bacterial challenge constituted time point 0 h.

NL1 (60 mg/kg) and gentamicin (1 mg/kg) were formulated for s.c. administration using PBS supplemented with 10% DMSO and 0.9 % saline as vehicles, respectively. All treatments and vehicles were delivered via s.c. injection on Day 0 immediately following the challenge. All mice (n=10/group) received two separate injections of 100 μL of the lead and antibiotic. NL1 and gentamicin were combined for Group 4. Mice were observed at least once daily during the pre-study phase and at least twice daily during the study period and sacrificed after observing signs of distress. Efficacy of test compounds was assessed by enumeration of animal survival over 19 days following instillation of infection.

Pediatric rat model

Long-Evans male rat pups (Crl:LE; Strain code: 006) were obtained from Charles River Laboratories (Cambridge, MA). Rat pups (n=13) received NL1 (40 mg/kg) via intraperitoneal (IP) injections twice a day for 5 days from P6-P10. Control animals (n=17) received vehicle treatments with DMSO (0.1%). IP injections were administered 12 h apart, and rat pups were weighed prior to each injection.

RNA-Seq

RNA-Seq libraries were prepared using NEBNext Ultra II directional RNA-Seq library prep kit (New England Biolabs). The libraries were sequenced using Illumina NextSeq 500 instrument in a paired-end 2×41 cycles setup. The number of paired end reads in samples ranged from 4 to 46 million. The reads were aligned against UCBPP-PA14 reference genome (pseudomonas.com) using bowtie2 version 2.4.1 (*96*). The number of reads in annotated genes was counted using htseq-count version 0.11.0 with option -i set to "gene_id" (*97*). The resulting count table was used for differential gene expression analysis with DESeq2 version 1.10.0 using Wald test (*98*).

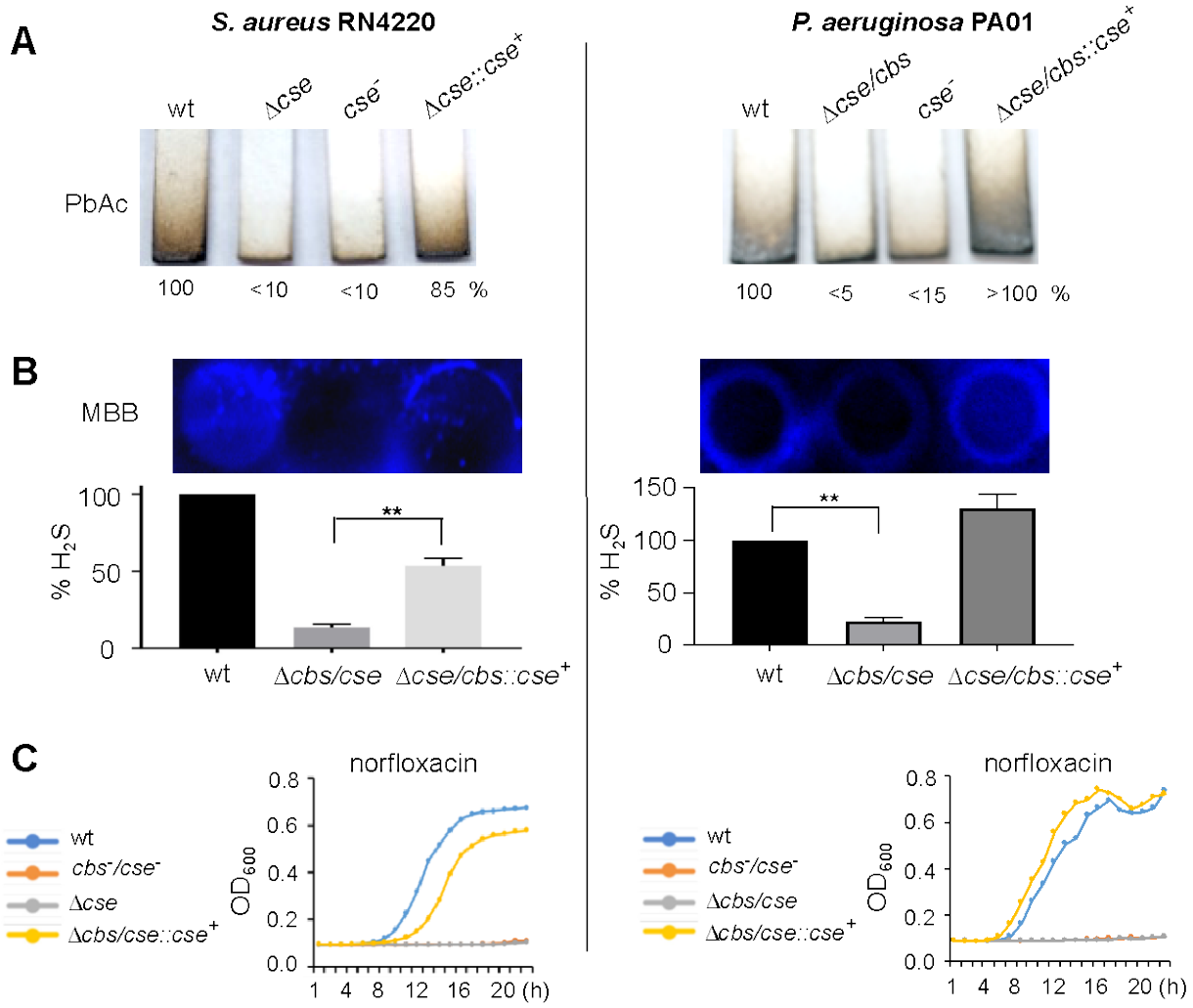

Fig. S1. bCSE is the predominant source of H_2S in *S. aureus* and *P. aeruginosa* (continuation of Fig. 1). Tn-based gene replacement (Δ) of *cbs* and/or *cse,* with or without *cse* complementation (+), were generated in *S. aureus* (RN4220) and *P. aeruginosa* (PAO1) (see Materials and Methods and Table S1) and compared to Tn insertions *cbs*/*cse(-)* mutants. (**A, B**) Quantitation of H_2S produced by wt and *cbs/cse* mutant strains. (**A**) Representative Pb-acetate-soaked paper strips affixed above the growth media level show a brown stain of PbS as a result of the reaction with gaseous H_2S exiting liquid bacterial cultures. Numbers indicate the H_2S production relative to wt cells. (**B**) Top: monobromobimane (MBB)-soaked nitrocellulose membrane affixed above the growth media level shows a fluorescent signal as a result of the reaction with gaseous H_2S exiting liquid bacterial cultures. Bottom: Quantification of the fluorescence signal. Values are means ± SD (n = 3), **P < 0.01 (Student's t-test; equal variance). (**C**) Representative growth curves of wt and *cbs/cse* mutants in the presence of norfloxacin (1 µg/ml). The data points are averages of optical density (OD) at 600 nm wavelength with a margin of error of less than 5%.

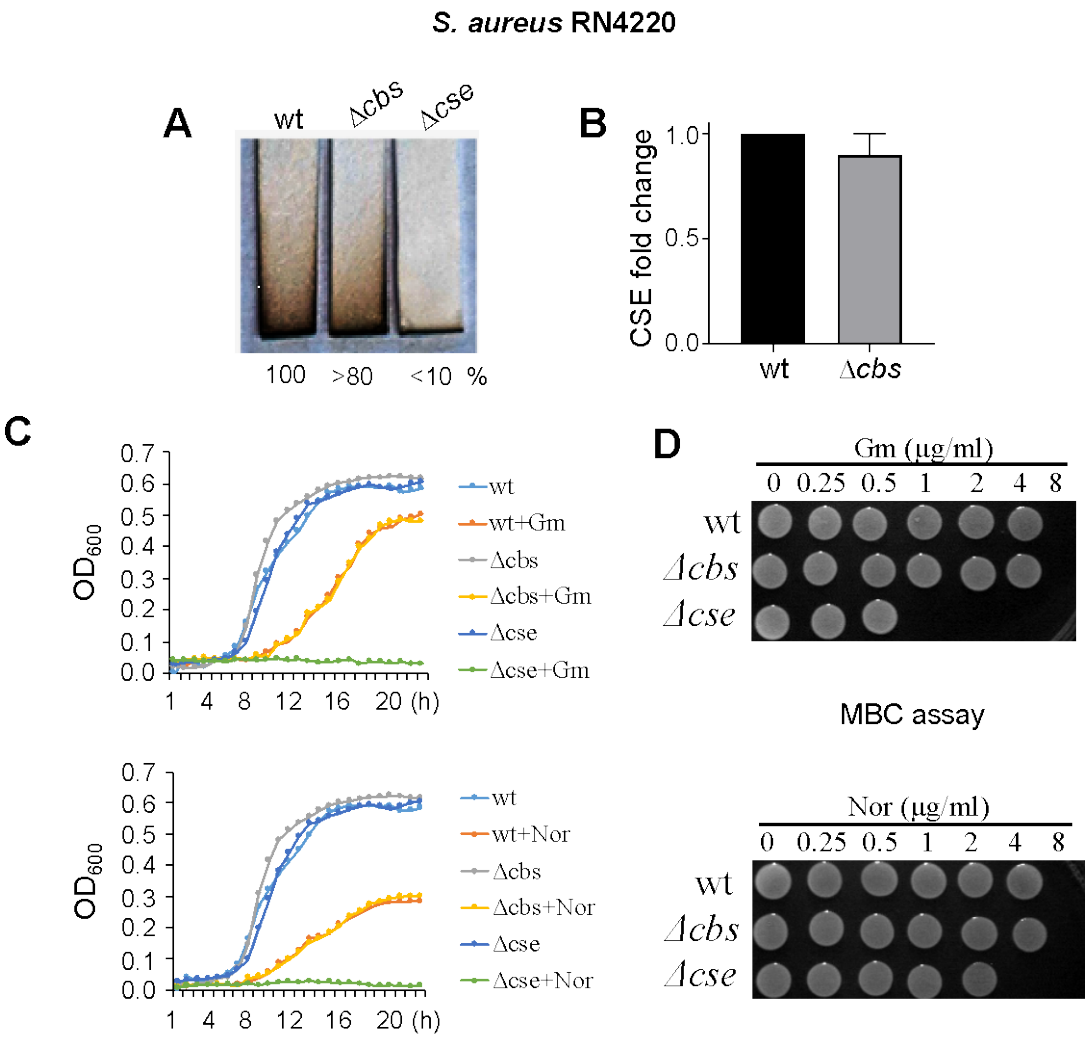

Fig. S2. bCBS contribution to H_2S production and resistance to antibiotics in *S. aureus* is not significant comparing to bCSE (continuation of Fig. 1). **(A)** Quantitation of H_2S produced by wt (RN4220), Δ*cbs,* and Δ*cse* mutant strains (see Table S1). Representative Pb-acetate-soaked paper strips affixed above the growth media level show a brown stain of PbS as a result of the reaction with gaseous H_2S exiting liquid bacterial cultures. Numbers indicate the H_2S production relative to wt cells. (**B**) The deletion of *cbs* did not change the expression of *cse* significantly from the wt level, as detected by RT-qPCR. Values are means ± SD (n = 3). (**C**) Representative growth curves of wt, Δ*cbs,* and Δ*cse* mutants in the presence of gentamycin (Gm; 2 μg/ml) and norfloxacin (Nor; 1 μg/ml). The data points are averages of optical density (OD) at 600 nm wavelength with a margin of error of less than 5%. (**C**) Illustrative efficiencies of colony formation from MBC experiments (see also **Table S3** and Methods).

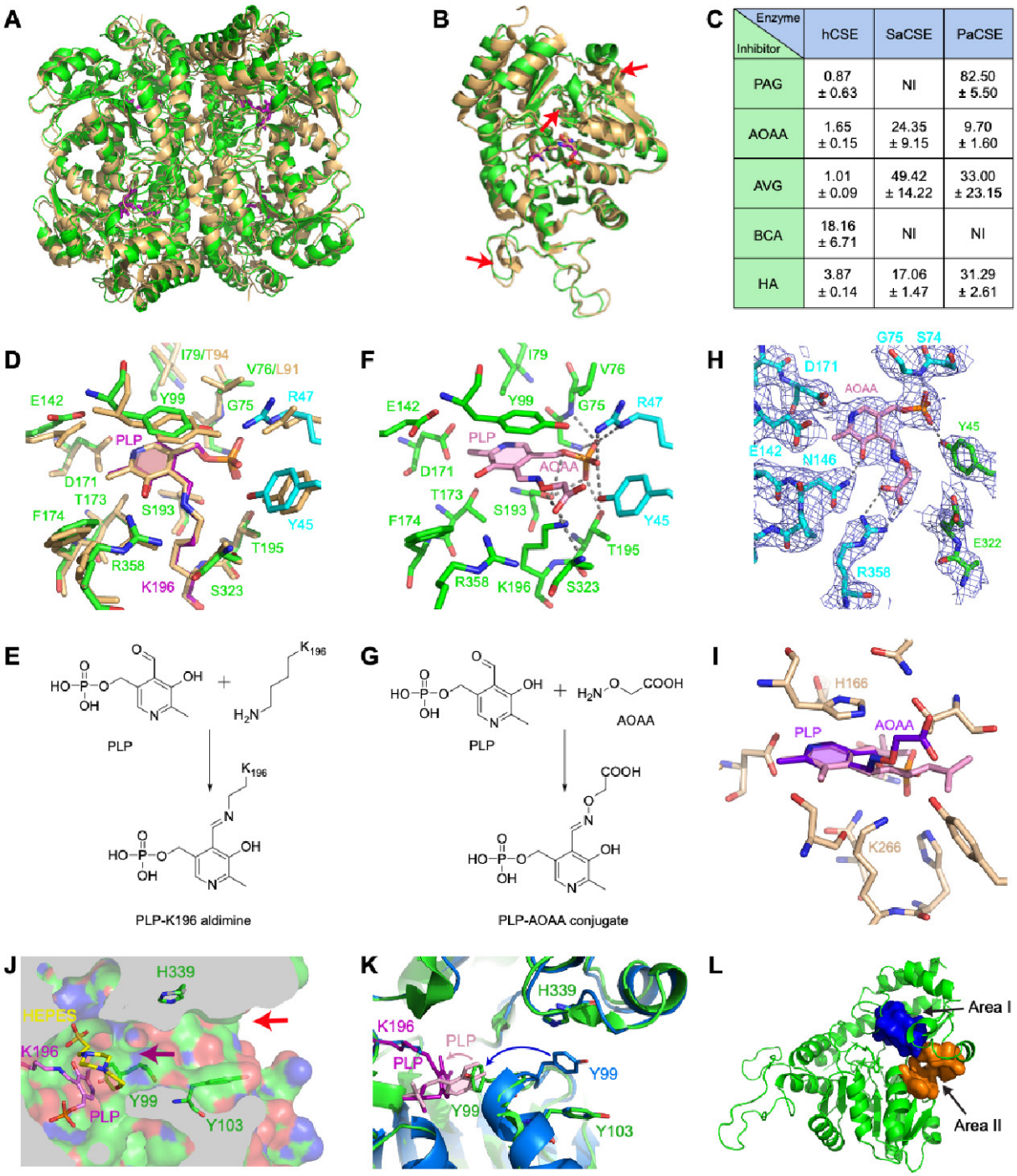

Fig. S3. Crystal structures of *S. aureus* CSE (SaCSE) and inhibition by conventional inhibitors. (**A-B**) All-atom superposition of *S. aureus* (green) and human (light orange, PDB: 2COG) CSE tetramers (A) and monomers (B). The PLP-K196 conjugate from SaCSE is in violet. Red arrows indicate major conformational differences. SaCSE tetramer is built using crystal symmetry. (**C**) Inhibition of CSEs by conventional inhibitors. IC_{50} values (mean ± SE, n=2) are in μM. Representative curves are in Fig. S2. NI, no inhibition. (**D**) Superposition between dimers of *S. aureus* (green and cyan) and human (light orange) CSEs centered on the catalytic site. The PLP-

lysine conjugates (violet for SaCSE) bind to two protomers. Numbering refers to SaCSE residues (green) and amino acids distinct in human CSE (orange). (**E**) Schematic of PLP and K196 conjugation resulting in the internal aldimine. (**F**) Catalytic site of SaCSE with PLP-AOAA conjugate (pink). Gray dashed lines depict putative hydrogen bonds (distance <3.5 Å). (**G**) Schematic of PLP and AOAA conjugation resulting in the external aldimine. AOAA mimics a reaction substrate and inhibits catalysis by preventing PLP-K196 conjugation. (**H**) $2F_o$-F_c simulated-annealing composite omit (SACO) map (1 σ level, blue mesh) shown with the final structural model around AOAA in the second SaCSE molecule of the asymmetric unit. (**I**) The catalytic site of *Thermus thermophilus* glycine decarboxylase (PDB ID 1WYV) with the PLP-AOAA conjugate (purple) superposed using ring atoms on the equivalent conjugate (pink) from SaCSE. Note different conformations of AOAAs and little similarity between the active sites of the enzymes. (**J**) Cross-section through the substrate entry tunnel (purple arrow) and the crevice (red arrow) in the crystal structures of SaCSE with the PLP-K196 conjugate (violet) and bound HEPES (yellow). (**K**) SaCSE in two conformations. The structure with the PLP-K196 conjugate (purple) is in green. The structure with the bound PLP prior to conjugation (light pink) in blue. Blue and pink arrows show movement of Y99 and the PLP ring upon formation of the holoenzyme. (**L**) Predicted druggable areas in SaCSE.

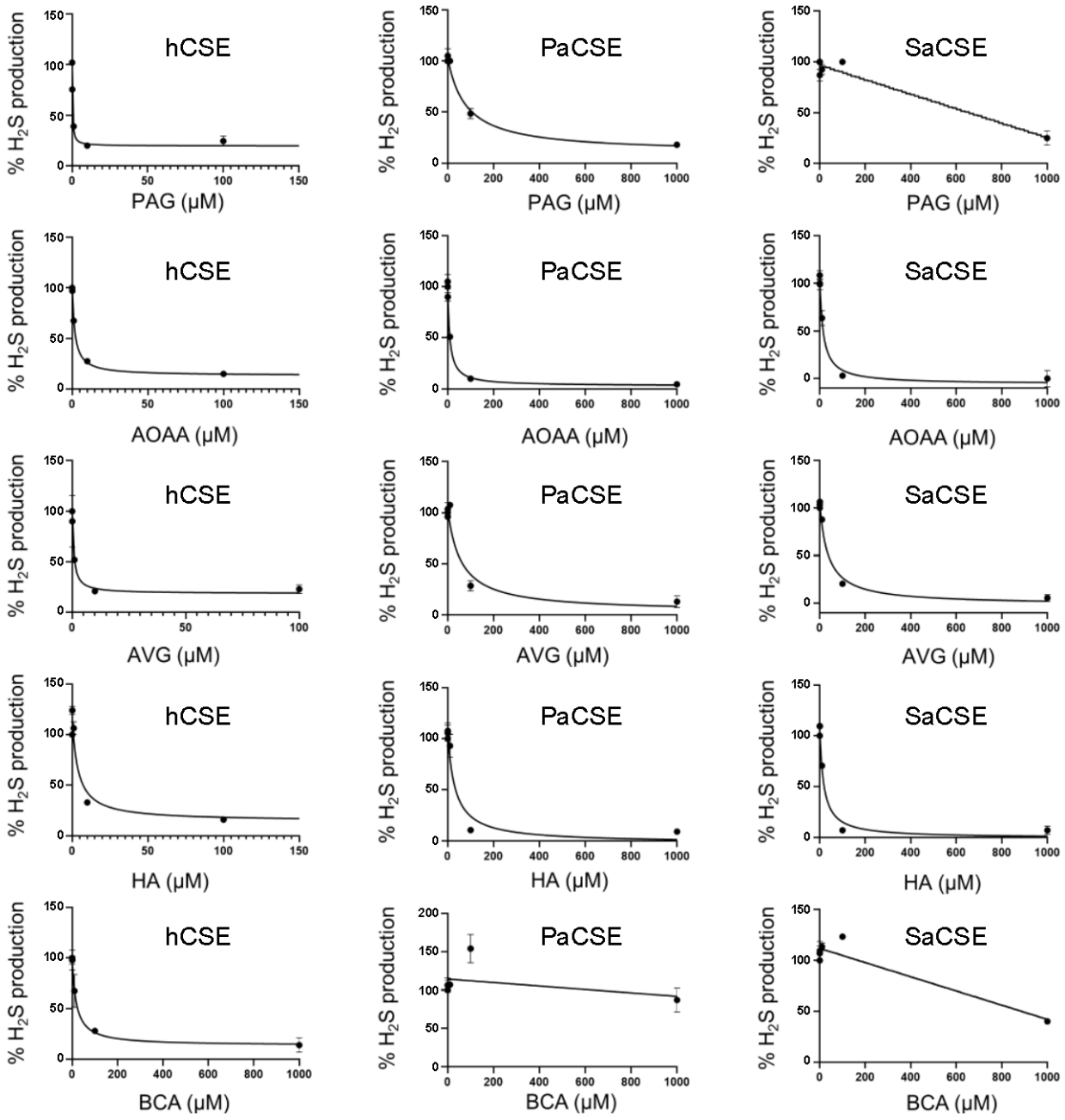

Fig. S4. Inhibition of CSEs by conventional inhibitors. Representative curves demonstrate the inhibition of H_2S production by purified *S. aureus* bCSE (SaCSE), *P. aeruginosa* (PaCSE) and human CSE (hCSE) as a function of inhibitor concentration. H_2S was detected by WSP5 fluorescent probe. The data were fit by non-linear regression to the Dose-response - Inhibition model; [Inhibitor] vs response (three parameters), in GraphPad Prism 7. Straight lines are shown for experiments where data cannot be fit to the inhibition model, suggesting weak or no inhibition at the range of the inhibitor concentration used in the experiment. The error bars indicate standard deviation for 2 technical replicates in each experiment. The mean values of 2 independent experiments are listed in **Fig. S3C**.

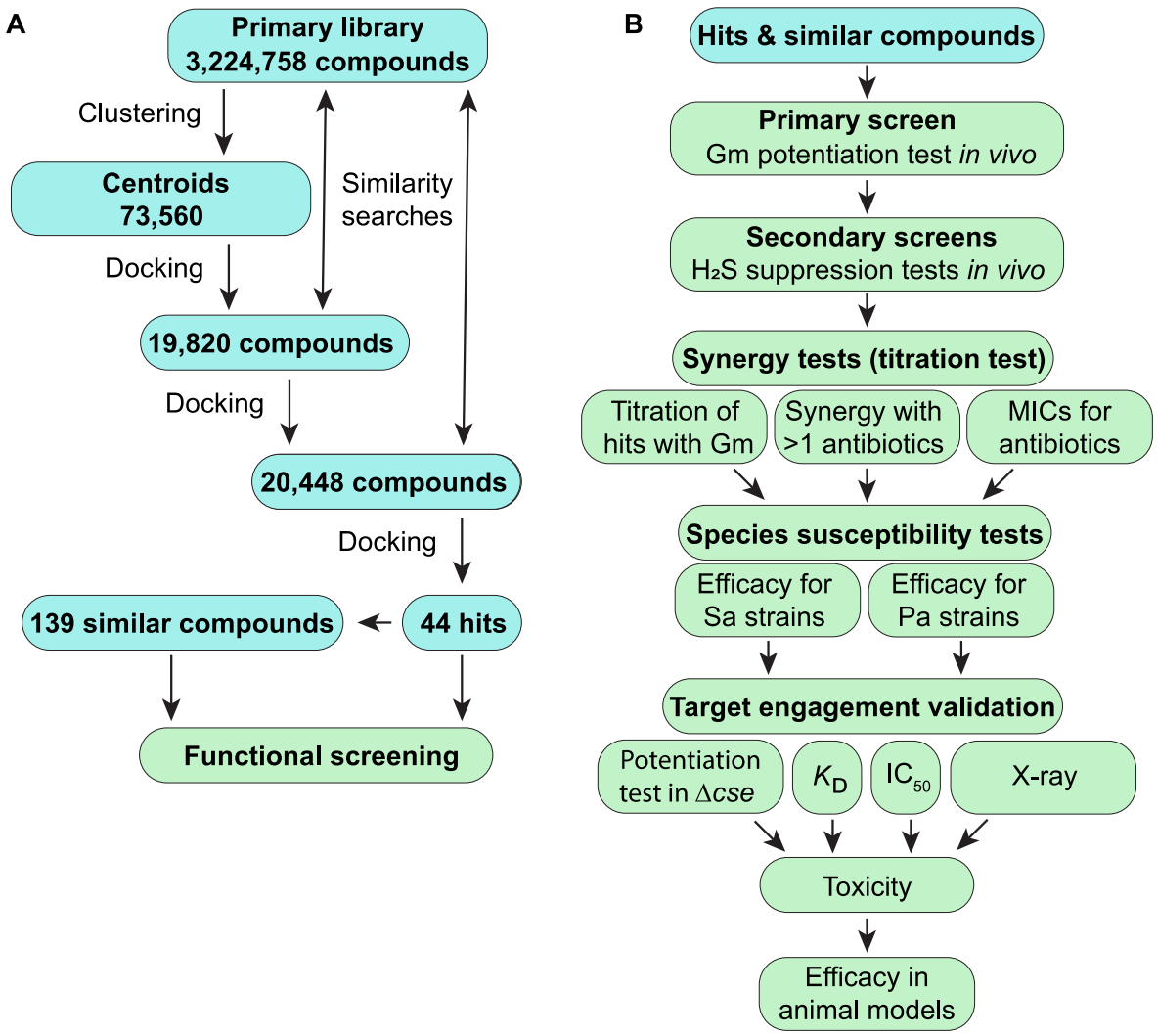

Fig. S5. Workflows of virtual screening and hit validation. (**A**) Schematics of the virtual screening workflow based on the structure of the SaCSE holoenzyme, crystallized in the *I*4122 space group with one protein molecule in the asymmetric unit. (**B**) Flow of activities for hit testing and validation in vitro and in vivo. The assays were: (1) primary screen: screening for potentiator compounds using 10 % MIC of Gm and *S. aureus* USA300 strain; (2) secondary screens: tests for suppression of H_2S biosynthesis in *S. aureus* USA300 strain using lead acetate strips and H_2S-specific WSP5 fluorescent sensor; (3) synergy tests: (i) determination of the minimal concentration of a hit compound to potentiate 10 % MIC of Gm, (ii) testing potentiation of hits with different antibiotics, (iii) determination of MICs for antibiotics with fixed concentrations of a hit; (4) species susceptibility tests: potentiation of different strains of *S. aureus* and *P. aeruginosa* with various hit/antibiotic combinations; (5) target engagement validation: (i) test for potentiation of Gm in *cse*(-) *S. aureus*, (ii) determination of binding affinity between a lead and CSEs using Microscale Thermophoresis (MST), (iii) determination of IC_{50} for inhibition of CSE activity by a lead using fluorescent H_2S detection assay in vitro; (iv) determination of X-ray crystal structures of SaCSE with bound leads; (6) toxicity test: the test with human cell line; (7) efficacy in animal models: survival of mice after *S. aureus* infection and *P. aeruginosa* burden in lungs of mice.

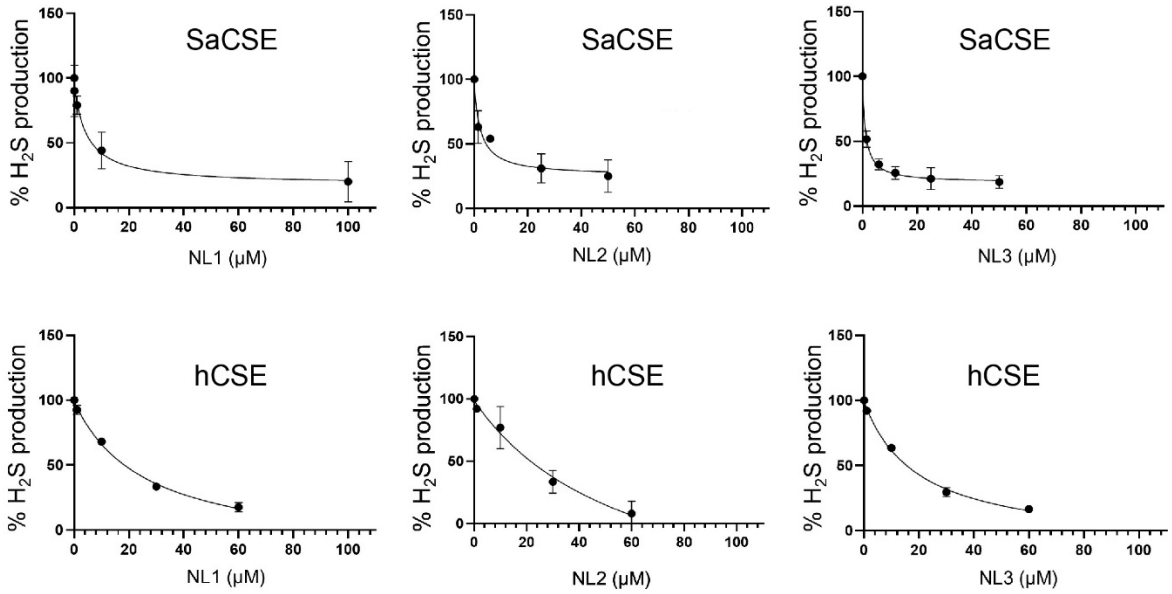

Fig. S6. Comparison of SaCSE and hCSE inhibition by NL1-3 compounds *in vitro*. Representative curves demonstrate the inhibition of H_2S production by purified *S. aureus* CSE (SaCSE) and human CSE (hCSE) as a function of NL1-3 concentration. H_2S was detected by WSP5 fluorescent probe. The data were fit by non-linear regression to the Dose-response - Inhibition model; [Inhibitor] vs response (three parameters), in GraphPad Prism 7. The error bars indicate standard deviation for 2 technical replicates in each experiment. The mean values of 2-4 independent experiments are listed in Fig. 2A.

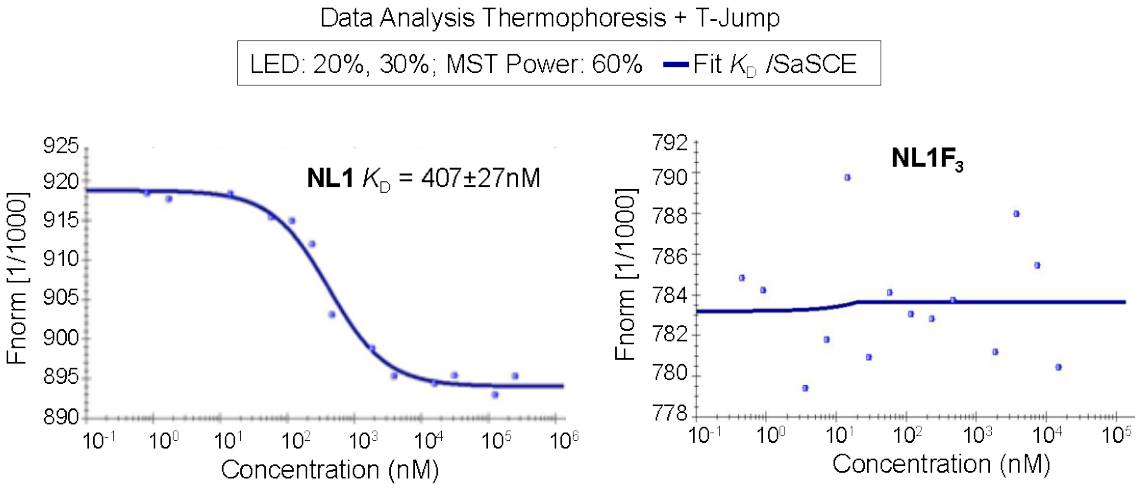

Fig. S7. bCSE interaction with NL1 and NL1F$_3$, measured by microscale thermophoresis (MST). To determine the binding affinity, a titration of a ligand was performed while the fluorescently labeled *S. aureus* bCSE was kept at a constant concentration. The change in the thermophoretic signal corresponds to a K_D = 407 ± 27 nM for NL1 (left panel). No binding was observed for NL1F$_3$ within the 100 μM range (right panel). The error bars represent the SD of each data point calculated from three independent thermophoresis measurements.

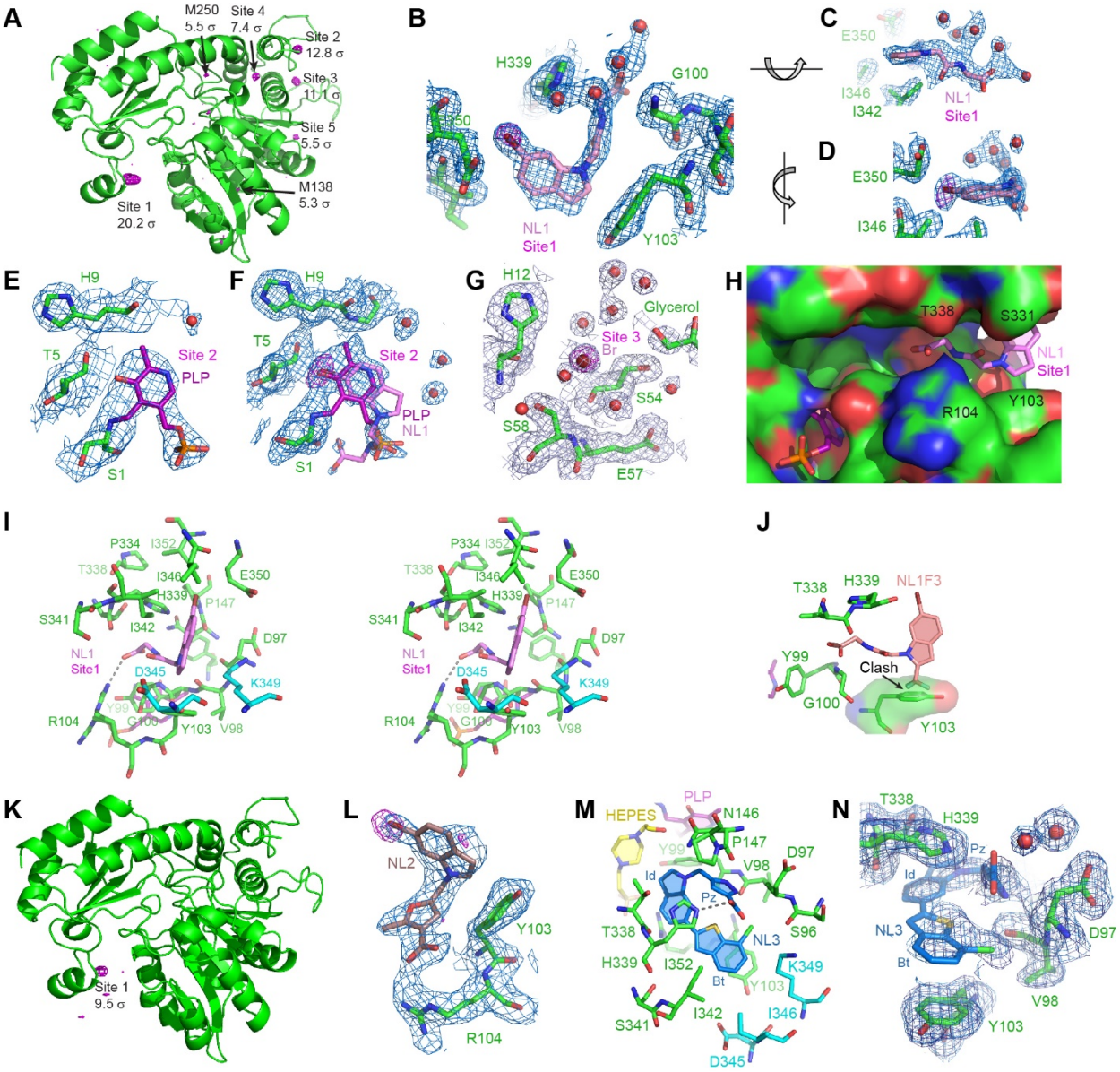

Fig. S8. SaCSE structures with bound leads and electron density maps. (**A**) Anomalous map (4.5 σ level, magenta mesh) shown with the NL1-bound structure. The maximal anomalous signal for Br atom in the NL1-binding sites and S atom of methionines are indicated in the labels. (**B-D**) Anomalous (5 σ, magenta) and $2F_o$-F_c SACO (1 σ, blue) maps shown with the refined structure (green) around NL1 (violet) in the major binding site (Site 1). Red spheres depict water molecules. Anomalous map unambiguously locates Br of NL1. (**E**) The N-terminal-linked PLP (purple) of the PLP-bound structure shown with the $2F_o$-F_c SACO map (1 σ, blue). (**F**) The minor NL1 binding site (Site 2) shown with the $2F_o$-F_c SACO (1 σ, blue) and anomalous (4 σ, magenta) maps and a mixture of NL1 and PLP at low occupancies. (**G**) The NL1 binding Site 3 shown with $2F_o$-F_c refined (1 σ, light blue) and anomalous (4 σ, magenta) maps. The maps for this and other minor sites allowed modelling of only Br atoms (brown spheres) of NL1. (**H**) NL1 binds in the crevice shown is surface representation. (**I**) A stereo view of NL1 binding in Site 1. This view is

perpendicular to the view in panel H. Symmetry-related CSE is in cyan. A gray dashed line depicts a putative hydrogen bond of NL1 with one of the alternative conformations of the Arg104 side chain. Flexibility of this amino acid argues against its importance for NL1 binding. (**J**) A structure-based model of NL1F3 binding that shows the -CF3 moiety clashing with Y103 (in surface representation). (**K**), Anomalous map (5 σ, magenta) shown with the NL2-bound structure. (**L**), NL2 (brown) shown with the $2F_o$-F_c SACO (1 σ, blue) and anomalous (5 σ, magenta) maps. (**M**) Details of NL3 binding. Benzothiophene (Bt), indole (Id) and pyrazole (Pz) moieties of NL3 (blue) are indicated. (**N**) Superposition of $2F_o$-F_c SACO maps (1 σ, blue and dark blue) from two crystals with NL3.

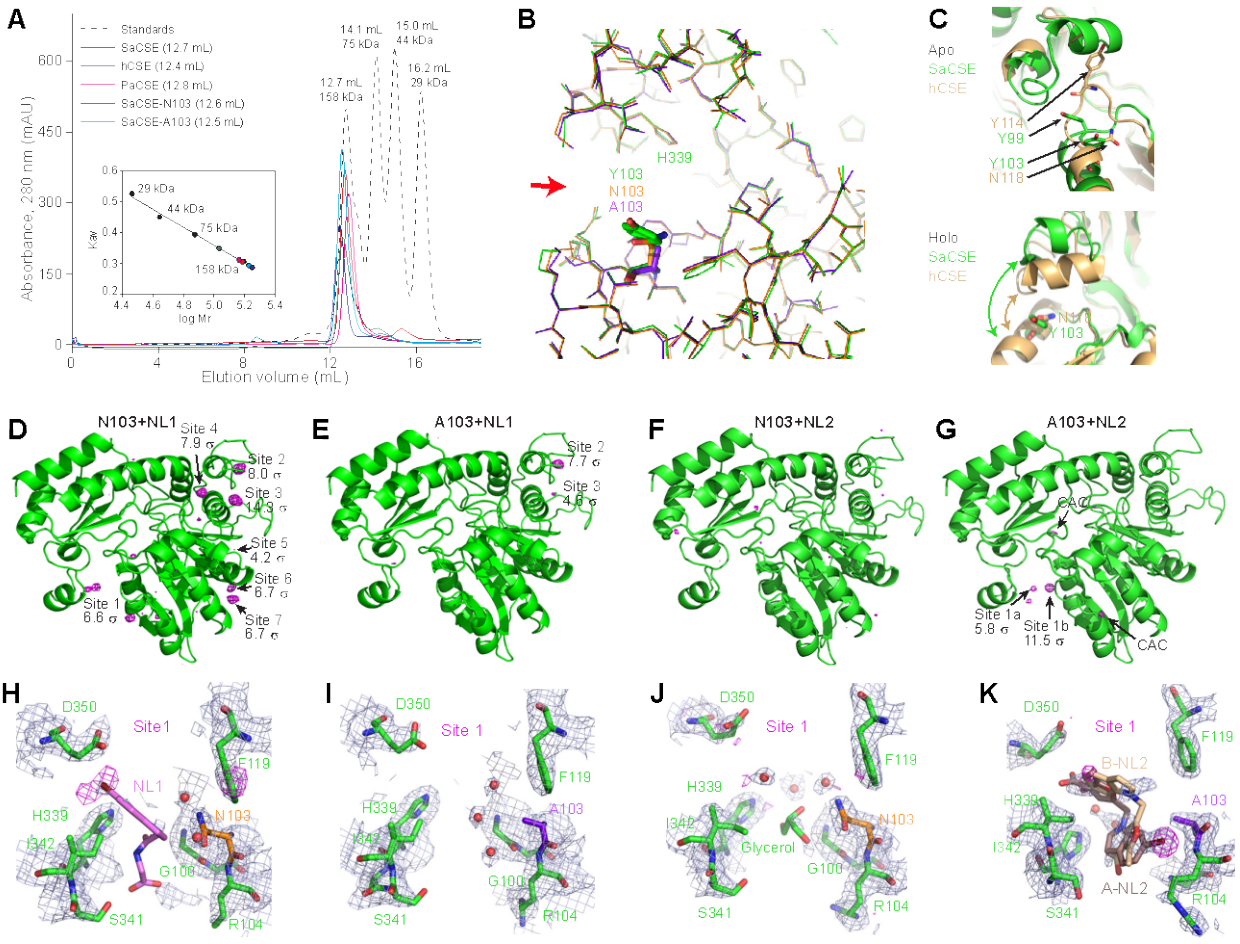

Fig. S9. Activity, assembly, structures and electron density maps of *S. aureus* CSE mutants. (**A**) Gel-filtration chromatography of wild type CSEs, SaCSE mutants, and protein standards. Inset, estimation of molecular weight (Mr) of protein assemblies based on a standard curve (solid line) as described in Materials and Methods. (**B**) All-atom superposition of the wild type (green) and Y103N (orange) and Y103A (purple) mutant structures of SaCSE centered on the lead binding pocket. Amino acids in position 103 are in sticks. Red arrow points at the crevice. (**C**) Superposition of hCSE (light orange) and SaCSE (green) in the apo (top) and holoenzyme (bottom) states. Top: a view around the crevice shows a largely disordered chain in hCSE (PDB: 3ELP) with Y114 (equivalent of Y99) moved up, away from N118 (equivalent of Y103). In SaCSE, Y99

is located closely to Y103. Bottom: the region becomes ordered in the hCSE holoenzyme (PDB: 2NMP) but the protein adopts a conformation without the open crevice while SaCSE has the crevice open for lead binding. (**D-G**) Structures of the Y103N (D, F) and Y103A (E, G) mutants co-crystallized with NL1 (D, E) and NL2 (F, G). The structures are shown with anomalous map (magenta mesh, 3.8, 4.2, 4.0, and 4.2 σ level, respectively). The maximal levels of anomalous signal for Br atom in the lead-binding sites are indicated in the labels. Anomalous signals without corresponding $2F_o$-F_c map or coinciding with non-anomalous scatters are considered background. Poor binding of NL1 in site 1 causes appearance of additional minor binding sites in (D). (**H-K**) Zoomed-in views on the lead binding site 1 in the structures of SaCSE mutants Y103N (H, J) and Y103A (I, K) co-crystallized with NL1 (H, I) and NL2 (J, K). The structures are shown with the refined $2F_o$-F_c (1 σ level, light-blue mesh) and anomalous (magenta mesh, 3.8, 4.2, 3.0, and 4.0 σ level, respectively) maps. Note poor $2F_o$-F_c map for NL1 (violet) (H); lack of both maps for NL1 in (I); lack of anomalous map and $2F_o$-F_c map sufficient to model glycerol in (J); and presence of two anomalous signals and islands of $2F_o$-F_c map sufficient to model NL2 in two conformations (A and B, brown and light brown) at low occupancy in (K).

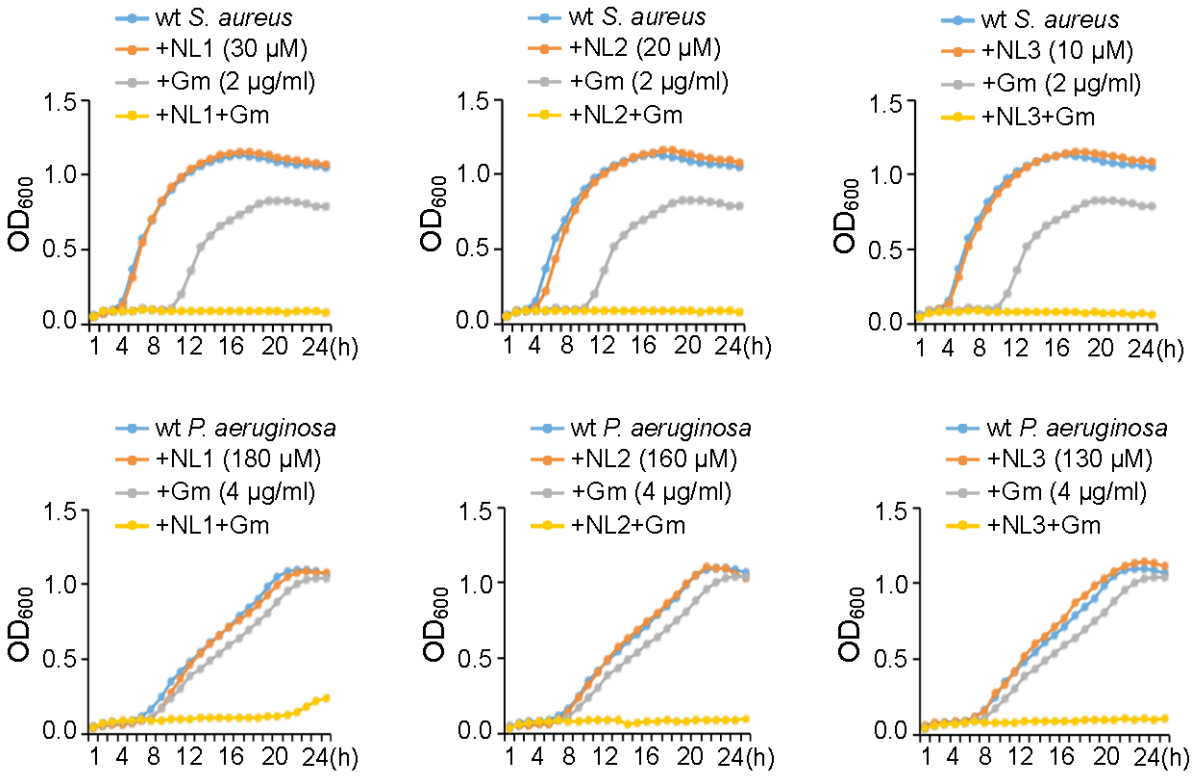

Fig. S10. Selected bCSE inhibitors do not affect bacterial growth at concentrations sufficient for Gm potentiation. Representative OD growth curves of *S. aureus* Newman (top panels) and *P. aeruginosa* PA14 (bottom panels) with the indicated amounts of Gm and NL1, NL2 and NL3. Cells were grown in triplicate at 37 °C with aeration using a Bioscreen C automated growth analysis system. The curves represent averaged values from three parallel experiments with a margin of error of less than 5%.

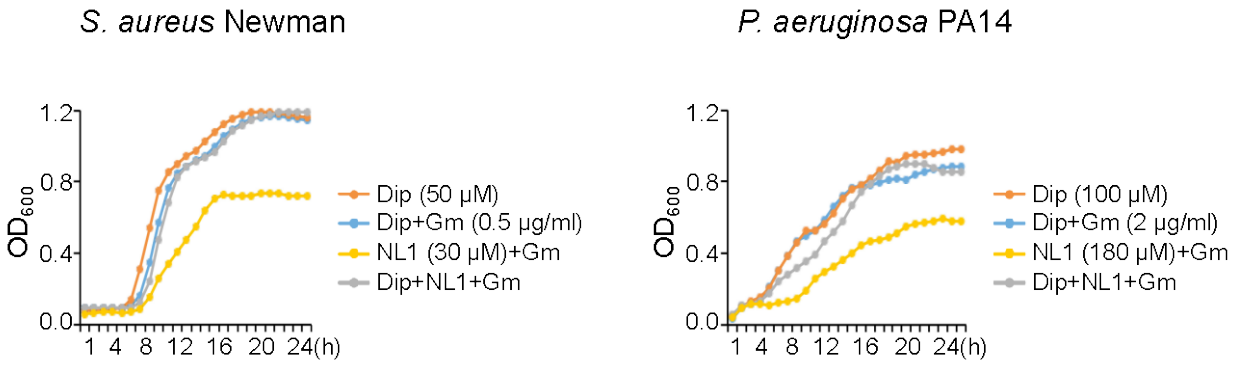

Fig. S11. Antibiotic potentiation with NL1 depends, at least in part, on Fenton chemistry. *S. aureus* Newman (left) and *P. aeruginosa* PA14 (right) cells were pretreated with the iron chelator, 2,2′-dipyridyl (Dip) for 3 min, followed by treatment with indicated amounts of Gm (blue) or Gm+NL1 (gray). Cells were grown in triplicate at 37 °C with aeration using a Bioscreen C automated growth analysis system. The curves represent averaged values from three parallel experiments with a margin of error of less than 5%.

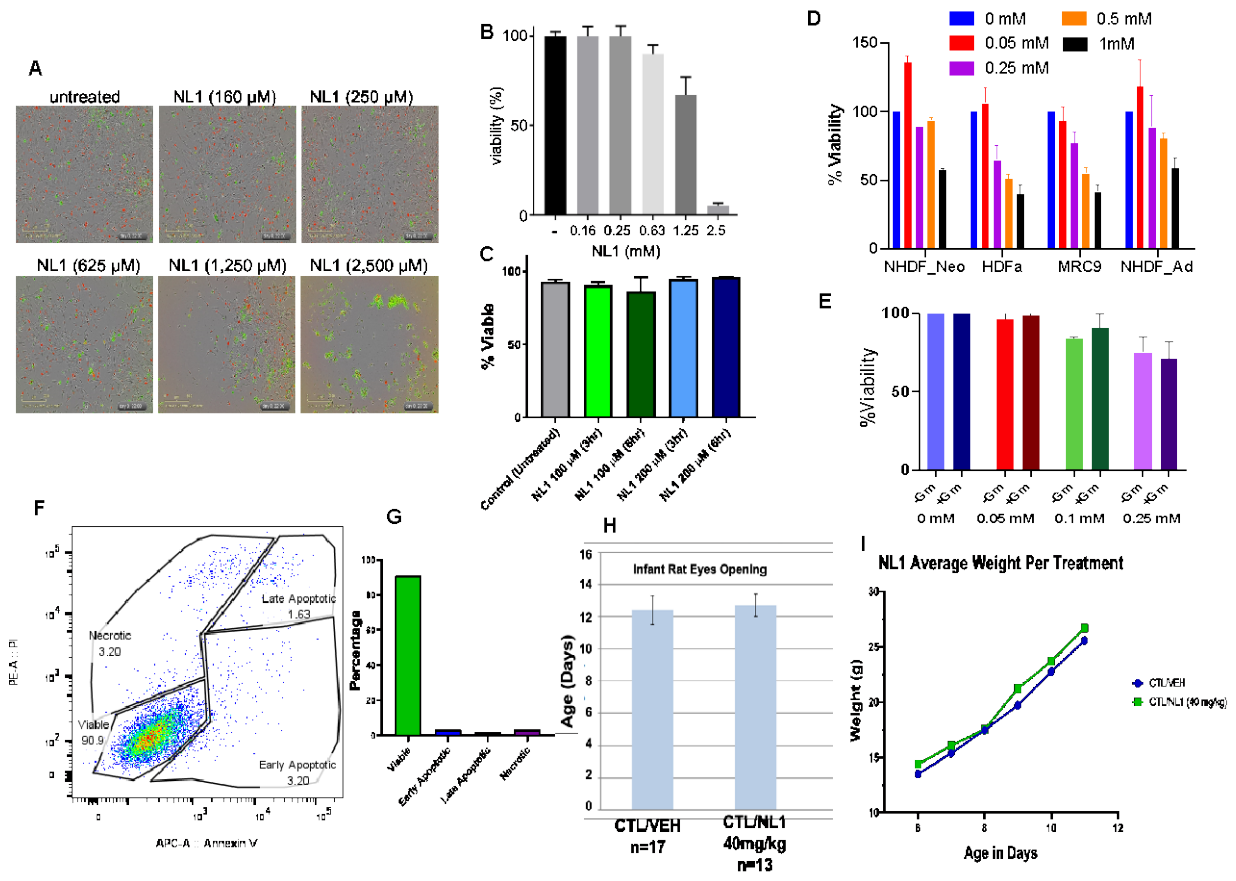

Fig. S12. **Safety profile of NL1**. (**A-E)** NL1 exhibits low cytotoxicity to human cells. **(A)** Human BJ fibroblast cell culture treated with a multiplex NucLight Red BacMam 3.0 reagent for nuclear staining of live cells (red) and the Cytotox Green reagent to detect dead cells (green). Concentrations of NL1 are indicated. Samples were imaged using Incucyte Zoom live-cell system. (**B)** Quantification of the viability data of Cytotox Green assay (mean ± SE, n=3). (**C**) Trypan blue exclusion assay following the incubation of human brain microvascular endothelial cells (HBMEC) with NL1 for the indicated time periods; percent viability was determined after recovery for 24 h. (**D)** Normal diploid human cell lines were continuously incubated with various concentrations of NL1 for 24 h, and cell viability was measured using CellTiter-Glo assay. (**E)** Diploid lung fibroblasts MRC9 were treated with NL1 with or without Gm (2 µg/ml) for 24 h and cell viability was measured using the CellTiter-Glo assay. No significant reduction in viability was observed due to Gm presence. (**F-G)** NL1 does not induce apoptosis: (**F**) HBMEC were treated with NL1 (200 µM) for 6 h. Cells were stained using the APC Annexin V Apoptosis Detection Kit with PI (BioLegend) and analyzed for apoptosis and necrosis using flow cytometry. (**G)** Quantification of the results from (F). (**H-I**) NL1 is safe in a chronic pediatric animal model: (H) Normal age window of eye opening. (**I**) Normal developmental weight in male rat pups treated with NL1 (40 mg/kg) compared to age matched controls receiving the vehicle. Rat pups (n=13) received NL1 via intraperitoneal injections (IP) twice a day for 5 days from P6-P10. Control animals (n=17) received vehicle treatments (DMSO 0.1%). IP injections were administered 12 h apart, and rat pups were weighed prior to each injection.

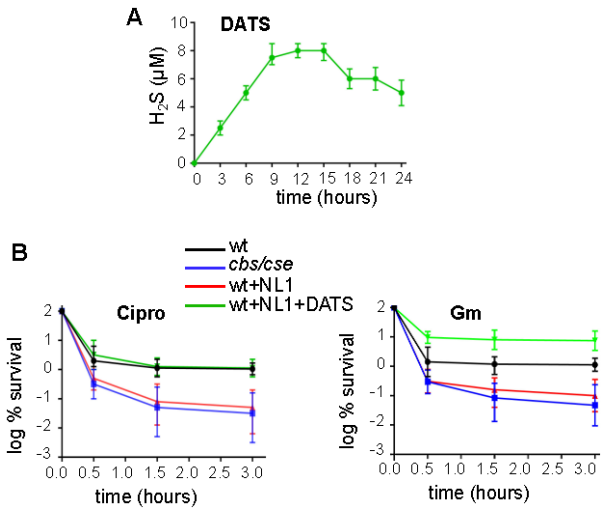

Fig. S13. **H_2S enhances antibiotic tolerance**. (**A**) Kinetics of spontaneous H_2S release from diallyl trisulfide (DATS) (1.4 mM) in LB as detected by WSP5 fluorescent H_2S probe using BioTek Cytation 3 instrument. (**B**) Exogenous H_2S suppresses the anti-persisters effect of bCSE inhibition. Changes in the viable cell density of exponentially growing wt and bCSE-deficient *S. aureus* Newman cultures challenged with 10 μg/ml ciprofloxacin (left) or 40 μg/ml gentamycin (right) are shown. WT cells were pretreated with 250 μM NL1 (red) or NL1+DATS (green). Data points are means ± SE (n=3).

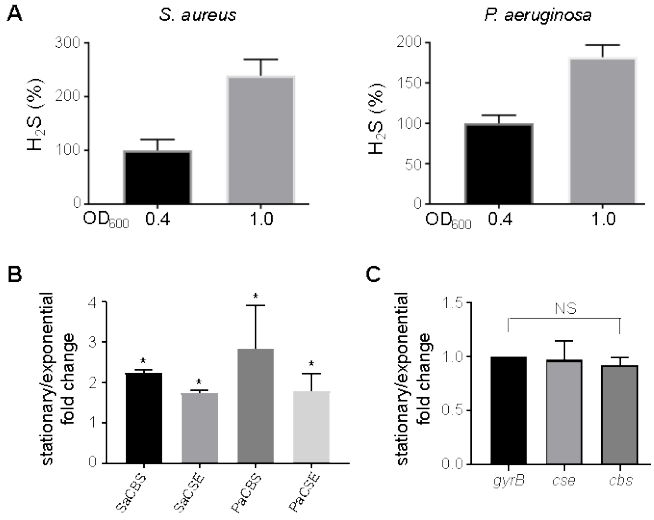

Fig. S14. **H_2S biosynthesis increases at the transition to the stationary phase.** (**A**) Relative amounts of H_2S generated by aerobically growing cultures of *S. aureus* Newman (left) and *P. aeruginosa* PA14 (right) in LB medium at the indicated OD_{600}, as detected by TICT-based fluorescent H_2S probe using Cytation 3 instrument. (**B**) Accumulation of bCBS and bCSE in *S. aureus* Newman (Sa) and *P. aeruginosa* PA14 (Pa) upon the transition to the stationary phase, as determined by LC-MS label-free quantitation using MaxQuant (see Methods). $^{*}P<0.05$. (**C**) No significant change in *cbs/cse* mRNA accumulation upon the transition to the stationary phase in *S. aureus* Newman, as determined by RT-qPCR. Values are means ± SD (n = 3), NS – nonsignificant.

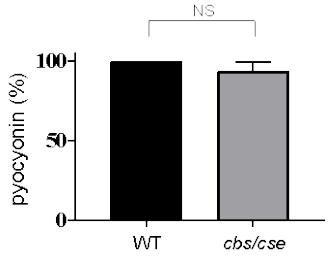

Fig. S15. **The total amount of pyocyanin in *P. aeruginosa* PA14 is unaffected by *cbs/cse* inactivation**. Pyocyanin was extracted from stationary cultures and quantified as described in the Methods. Values are means ± SD (n = 3), NS – nonsignificant.

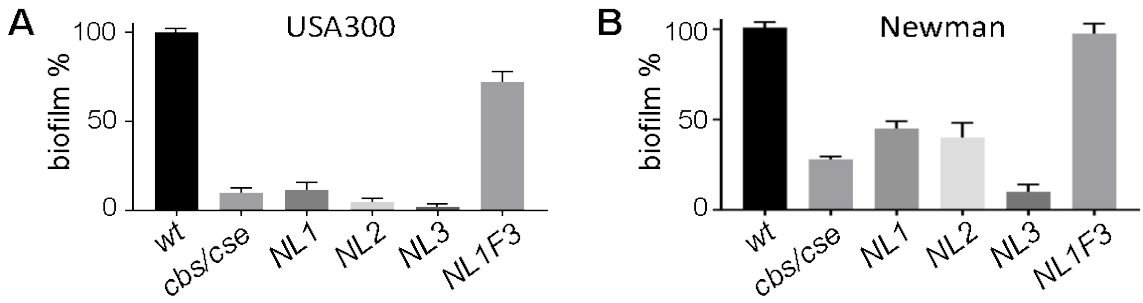

Fig. S16. **Genetic or chemical inactivation of bCSE compromises *S. aureus* USA300 (A) and Newman (B) biofilm formation**. The assay is essentially as described in the Methods for *P. aeruginosa*, except that the overnight cultures were diluted in 0.5×TSB supplemented with 1% glucose, and 50 µL crystal violet solution (0.06%, v/v) was added for 5 min.

Table S1. Strains, Cell lines and Plasmids

Strains, Plasmids, Cell Lines	Description	Source or reference
***S. aureus* strains**		
RN4220	WT	R. Novick
RN4220 Δ*cbs*	Δ*cbs*::aphA3 (Kan^R) gene replacement	This work
RN4220 Δ*cse*	Δ*cse*::aphA3 (Kan^R) gene replacement	This work
RN4220 *cse*(-)	*cse*::baIS (Em^R) gene disruption	This work
RN4220 Δ*cbs cse*(-)	Δ*cbs*::aphA3 (Kan^R) cse::baIS (Em^R)	This work
RN4220 Δ*cse cse*(+)	Δ*cse*::aphA3 (Kan^R) *cse* complementation	This work
RN450 lysogenic strain	Bacteriophage 80 gamma	R. Novick
USA300	WT MRSA (clinical isolate JE2)	R. Novick
USA300 Δ*cbs*	Δ*cbs* ::Kan^R	This work
USA300 *cbs*(-) *cse*(-)	*cbs*::baIS (Em^R) *cse*(-) due to polarity	This work
USA300 *cse*(-)	*cse*::baIS (Em^R)	This work
USA300 Δ*cbs cse*(-)	Δ*cbs*::aphA3 (Kan^R) *cse*::baIS (Em^R)	This work
Newman	WT	V. Torres
Newman Δ*cbs*	Δ*cbs*::aphA3 (Kan^R)	This work
Newman *cse*(-)	*cse*::baIS (Em^R)	This work
Newman Δ*cbs cse*(-)	Δ*cbs*::aphA3 (Kan^R) *cse*::baIS (Em^R)	This work
***P. aeruginosa* strains**		
PAO1	WT	U. Washington Tn collection
PAO1 *cbs*(-) *cse*(-)	*cbs*::phoA (Tc^R) gene disruption; *cse*(-) due to polarity	U. Washington Tn collection
PAO1 *cse*(-)	*cse*::hahIS (Tc^R) gene disruption	U. Washington Tn collection
PAO1 Δ*cbs* Δ*cse*	Δ*cbs* Δ*cse* (markerless deletion)	Y. Xia
PAO1 Δ*cbs* Δ*cse*/ pUCP24:paCSE	Δ*cbs* Δ*cse*/pUCP24:*cse* (Gm^R)	This work
PA14	WT	E. Drenkard
PA14 *cbs*(-) *cse*(-)	*cbs*:: MAR2xT7 (Gm^R); *cse*(-) due to polarity	E. Drenkard
***E. coli* strains**		
BL21(DE3)	*dcm ompT hsdS*($r_B^- m_B^-$) *gal* (DE3)	ThermoFisher scientific USA C600003
BL21 Star (DE3)	F- *ompT hsdSB* (rB - mB -) *gal dcm rne131* (DE3)	ThermoFisher scientific USA C6010-03
BL21 Star(DE3)/pSUMO:saCSE	*S. aureus* CSE expression strain	This work
BL21(DE3)/pNIC28-Bsa4	Human CSE expression strain	This work
BL21 Star(DE3)/pSUMO:saCSE (H339A)	*S. aureus* H339A mutant CSE expression strain	This work
BL21 Star(DE3)/pSUMO:saCSE (Y103A)	*S. aureus* Y103A mutant CSE expression strain	This work

BL21 Star(DE3)/pSUMO:saCSE (Y103N)	*S. aureus* Y103N mutant CSE expression strain	This work
BL21 Star(DE3)/pSUMO:paCSE	*P. aeruginosa* CSE expression strain	This work
Plasmids		
pSUMO	Expression vector with 10X His-tag	Addgene 54336 modified by H. Li
pSUMO:saCSE	*S. aureus* CSE expression vector	This work
pNIC28-Bsa4	Human CSE expression vector	Addgene 42365
pSUMO:paCSE	*P. aeruginosa* CSE expression vector	This work
pSUMO:saCSE (H339A)	*S. aureus* CSE H339A mutant expression vector	This work
pSUMO:saCSE (Y103A)	*S. aureus* CSE Y103A mutant expression vector	This work
pSUMO:saCSE (Y103N)	*S. aureus* CSE Y103N mutant expression vector	This work
pUCP24	*E. coli-P. aeruginosa* shuttle vector	O. Zaborina
pUCP24:paCSE	*P. aeruginosa* CSE expression vector	This work
pKS1	shuttle vector	(*67*)
pKS1:saCSE	*S. aureus* CSE deletion vector	This work
pKS1:saCBS	*S. aureus* CBS deletion vector	This work
Cell Lines		
BJ-5ta	Normal human foreskin fibroblast	ATCC CRL-4001
NHDF	Normal Human Dermal Fibroblast Neonatal	Lonza CC-2509
NHDF	Normal Human Dermal Fibroblast Adult	Lonza CC-2511
HDFa	Human dermal fibroblast	ATCC PCS-201-012
MRC9	Normal human lung fibroblast	ATCC CCL-212
HBMEC	Human Brain Microvascular Endothelial Cells	Cell Systems ACBRI 376

Table S2. MICs of antibiotics in the presence and absence of selected bCSE inhibitors.

			MIC (μg/ml)						
			wt					*cse*(-)	
Antibiotic	**Strain**	**Inhibitor:** (μM *Sa*/*Pa*)	**-**	**NL1** 30/180	**NL2** 20/160	**NL3** 10/130	**NL1F$_3$** 180	**-**	**NL1** 30/180
Gentamycin	*S.aureus* RN4220		4.0	1.6	0.8	0.3	4.0	1.2	1.0
	S.aureus Newman		8.0	4.0	4.0	3.0	8.0	3.0	3.0
	S.aureus USA300		4.0	2.0	2.0	2.0	4.0	2.0	2.0
	P. aeruginosa PAO1		4.0	2.0	2.5	3.0	4.0	1.5	1.5
	P. aeruginosa PA14		2.0	1.0	1.0	2.0	2.0	--	--
Kanamycin	*S. aureus* USA300		25	5.0	5.0	2.5	25	10	10
Norfloxacin	*S.aureus* RN4220		2.0	1.0	1.0	0.5	1.0	0.25	0.25
	P. aeruginosa PA14		0.8	0.4	0.4	0.6	0.8	0.3	0.3
Ciprofloxacin	*S. aureus* RN4220		1.0	0.5	0.5	0.5	--	0.5	0.5
	P. aeruginosa PA14		0.1	0.04	0.06	0.06	--	0.04	0.04
Ampicillin	*P. aeruginosa* PA14		200	100	100	100	200	100	100
Carbenicillin	*P. aeruginosa* PAO1		360	250	300	300	--	180	180
Methicillin	*S. aureus* USA300		25	12.5	12.5	10	25	12.5	12.5
Vancomycin	*S. aureus* RN10659		3.0	1.5	1.5	1.0	--	--	--
Chloramphenicol	*S. aureus* RN4220		3.0	3.0	3.0	3.0	3.0	3.0	3.0
	P. aeruginosa PA14		50	50	50	50	50	50	50
Tetracycline	*S. aureus* RN4220		0.02	0.02	0.02	0.02	0.02	0.02	0.02

Bactericidal and bacteriostatic antibiotics are indicated by gray and white background, respectively. Sa/Pa – *S. aureus*/*P. aeruginosa.*

Table S3. MBCs of antibiotics in the presence and absence of selected bCSE inhibitors.

			MBC (μg/ml)						
			wt					*cse*(-)	
Antibiotic	**Strain**	**Inhibitor:** (μM *Sa*/*Pa*)	**-**	**NL1** 30/180	**NL2** 20/160	**NL3** 10/130	**NL1F$_3$** 180	**-**	**NL1** 30/180
Norfloxacin	*S. aureus* RN4220		8.0	4.0	4.0	2.0	8.0	4.0	4.0
	P. aeruginosa PA14		6.4	3.2	3.2	6.4	6.4	3.2	3.2
Ampicillin	*S. aureus* RN4220		0.8	0.8	0.8	0.1	--	0.4	0.4
	P. aeruginosa PA14		400	100	150	50	--	200	200
Gentamicin	*S. aureus* RN4220		8.0	1.0	1.0	0.5	8.0	1.0	1.0
	P. aeruginosa PA14		10	5.0	5.0	5.0	10	--	--

Table S4. X-ray crystallography data collection and refinement statistics, PLP-bound, PLP-conjugated and AOAA-bound SaCSE structures.

Data collection					
Data set	PLP bound	Holoenzyme	Holoenzyme High HEPES	Holoenzyme Dimer	AOAA-bound Dimer
Wavelength (Å)	0.91956	0.92010	0.91956	0.91956	0.91956
Space group	*I*4122	*I*4122	*I*4122	*P*4322	*P*4322
Cell dimensions					
a, b, c (Å)	104.96, 104.96, 289.56	105.13, 105.13, 288.15	104.28, 104.28, 287.68	104.46, 104.46, 286.60	104.35, 104.35, 287.36
α, β, γ (°)	90.00 90.00 90.00	90.00 90.00 90.00	90.00 90.00 90.00	90.00 90.00 90.00	90.00 90.00 90.00
Resolution (Å)	20.00–2.40 (2.45–2.40)[a]	30.00–2.14 (2.19–2.14)[a]	30.00–2.52 (2.58–2.52)[a]	30.00–2.40 (2.44–2.40)[a]	30.00–2.85 (2.90–2.85)[a]
R_{merge}[b]	0.194 (1.244)	0.099 (1.084)	0.152 (0.997)	0.219 (1.157)	0.200 (1.056)
R_{pim}[c]	0.062 (0.492)	0.023 (0.256)	0.033 (0.211)	0.054 (0.291)	0.061 (0.316)
$CC_{1/2}$	0.996 (0.608)	0.999 (0.955)	0.999 (0.979)	0.992 (0.872)	0.990 (0.845)
$I/\sigma(I)$	7.0 (0.8)	23.7 (3.3)	19.3 (4.0)	2.3 (0.3)	2.6 (0.5)
Completeness (%)	99.9 (98.3)	99.8 (97.5)	99.8 (98.4)	100 (100)	100 (100)
Redundancy	10.5 (6.6)	18.7 (18.1)	22.6 (22.5)	17.2 (16.5)	11.7 (12.0)
No. unique reflections	31,961 (1,811)	45,133 (3,211)	27,451 (1,944)	63,162 (3,103)	38,274 (1,874)
Refinement					
Resolution (Å)	19.96 – 2.40	29.39 – 2.14	29.60 – 2.51	29.76 – 2.40	29.76 – 2.84
R_{work}/ R_{free} (%)	18.1/21.4	16.2/18.4	16.4 /18.9	14.9/17.3	17.7 /20.9
No of atoms					
Protein	2,844	2,928	2,921	5,818	5,797
Lead	-	-	-	-	-
Other ligands[d]	27	40	55	57	66
Water	149	248	156	496	87
Average B-factors ($Å^2$)					

Protein	45.11	41.30	44.66	35.32	42.20
Lead	-	-	-	-	-
Ligand	56.28	56.42	58.66	49.50	47.74
Water	46.34	49.02	48.20	41.50	42.81
R.m.s deviations					
Bond lengths (Å)	0.008	0.007	0.006	0.007	0.008
Bond angles (°)	0.984	0.849	0.904	0.951	1.057
Ramachandran analysis					
Favored (%)	96.50	97.07	97.33	96.93	95.63
Allowed (%)	3.50	2.93	2.67	3.07	4.23
Outliers (%)	0.00	0.00	0.00	0.00	0.13
Clash score	3.49	2.54	3.54	2.82	5.74
PDB code	7MCL	7MCB	7MCN	7MCP	7MCQ

[a]The highest-resolution shell values are shown in parentheses.

[b]$R_{merge} = \Sigma_h \Sigma_i | I(h)_i - < I(h) > | / \Sigma_h \Sigma_i I(h)_i$, where $I(h)$ is the intensity for reflection h, Σ_h is the sum for all reflections, and Σ_i is the sum for i measurements of reflection h.

[c]$R_{pim} = \Sigma_{hkl} \sqrt{(1/(n-1))} \Sigma_i | I(hkl)_i - <I(hkl)> | / \Sigma_{hkl} \Sigma_i I(hkl)_i$

[d]Ligand indicates components of the crystallization solution (buffer, cations, etc.) except lead or drug molecules.

Table S5. X-ray crystallography data collection and refinement statistics, SaCSE holoenzyme co-crystallized with lead H_2S inhibitors.

Data collection				
Data set	+ NL1	+ NL2	+ NL3	+ NL1F3
Wavelength (Å)	0.91887	0.91956	0.92013	0.91956
Space group	*I*4122	*I*4122	*I*4122	*I*4122
Cell dimensions				
a, b, c (Å)	105.11, 105.11, 288.10	104.89, 104.89, 288.27	105.44, 105.44, 287.77	104.79, 104.79, 287.86
α, β, γ (°)	90.00 90.00 90.00	90.00 90.00 90.00	90.00 90.00 90.00	90.00 90.00 90.00
Resolution (Å)	30.00–1.60 (1.64–1.60)[a]	29.00–2.40 (2.46–2.40)[a]	30.00–1.72 (1.75–1.72)[a]	30.00–2.12 (2.16–2.12)[a]
R_{merge}[b]	0.114 (2.558)	0.142 (0.361)	0.117 (0.846)	0.247 (0.777)
R_{pim}[c]	0.025 (0.585)	0.042 (0.142)	0.031 (0.288)	0.061 (0.230)
$CC_{1/2}$	1.00 (0.803)	0.993 (0.919)	0.998 (0.826)	0.967 (0.871)
$I/\sigma(I)$	19.9 (1.4)	2.2 (0.4)	20.3 (1.4)	7.9 (0.7)
Completeness (%)	99.6 (95.5)	97.4 (77.3)	99.4 (89.8)	99.8 (97.8)
Redundancy	22.1 (19.4)	11.3 (5.4)	14.4 (6.3)	16.6 (8.7)
No. unique reflections	106,360 (7,458)	31,024 (1,723)	85,730 (3,829)	45,500 (2,197)
Refinement				
Resolution (Å)	29.71 – 1.60	28.94 – 2.40	29.71 – 1.72	29.66 – 2.12
R_{work}/ R_{free} (%)	16.2/17.2	15.7/19.4	15.8/16.4	17.1/19.7
No of atoms				
Protein	2,933	2,946	2,974	2,915
Lead	39	20	28	-
Other ligands[d]	43	48	54	62
Water	448	226	450	234
Average B-factors (Å^2)				
Protein	27.56	34.36	22.52	37.00

Lead	48.95	57.89	52.80	-
Ligand	47.63	54.27	47.21	49.28
Water	41.42	37.07	37.10	44.33
R.m.s deviations				
Bond lengths (Å)	0.006	0.007	0.007	0.007
Bond angles (°)	0.832	0.941	0.992	0.907
Ramachandran analysis				
Favored (%)	97.87	97.07	97.60	97.33
Allowed (%)	2.13	2.93	2.40	2.67
Outliers (%)	0.00	0.00	0.00	0.00
Clash score	1.51	3.18	2.33	4.73
PDB code	7MCT	7MCU	7MCY	7MD0

[a]The highest-resolution shell values are shown in parentheses.

[b-d]R_{merge}, R_{pim} and ligand details are given in the footnote to Table S4

Table S6. X-ray crystallography data collection and refinement statistics mutated SaCSE holoenzyme co-crystallized with and without lead H_2S inhibitors.

Data collection						
Data set	Y103N mutant	Y103N mutant + NL1	Y103N mutant + NL2	Y103A mutant	Y103A mutant + NL1	Y103A mutant + NL2
Wavelength (Å)	0.91956	0.91956	0.91956	0.91956	0.91956	0.91956
Space group	I4122	I4122	I4122	I4122	I4122	I4122
Cell dimensions						
a, b, c (Å)	105.26, 105.26, 288.30	104.37, 104.37, 287.72	106.10, 106.10, 287.63	104.89, 104.89, 286.89	105.22, 105.22, 287.66	105.11, 105.11, 287.79
α, β, γ (°)	90.00 90.00 90.00	90.00 90.00 90.00	90.00 90.00 90.00	90.00 90.00 90.00	90.00 90.00 90.00	90.00 90.00 90.00
Resolution (Å)	30.00–2.30 (2.35–2.30)[a]	30.00–2.20 (2.24–2.20)[a]	30.00–2.06 (2.10–2.06)[a]	30.00–1.80 (1.84–1.80)[a]	30.00–2.24 (2.29–2.24)[a]	30.00–1.80 (1.83–1.80)[a]
R_{merge}[b]	0.162 (1.519)	0.186 (1.131)	0.262 (1.972)	0.092 (1.045)	0.241 (1.405)	0.104 (1.409)
R_{pim}[c]	0.047 (0.417)	0.047 (0.339)	0.066 (0.587)	0.035 (0.419)	0.066 (0.489)	0.037 (0.539)
$CC_{1/2}$	0.998 (0.909)	0.993 (0.833)	0.975 (0.485)	0.998 (0.851)	0.983 (0.697)	0.989 (0.748)
$I/\sigma(I)$	61.3 (6.5)	6.7 (0.6)	76.8 (5.9)	219.2 (12.4)	5.4 (0.1)	38.6 (1.6)
Completeness (%)	99.9 (100)	99.9 (98.4)	100 (99.6)	99.4 (100)	99.9 (99.4)	100 (99.9)
Redundancy	12.9 (13.9)	16.4 (11.1)	16.0 (9.4)	7.7 (7.2)	13.9 (8.4)	8.9 (7.3)
No. unique reflections	36,145 (2,375)	40,858 (2,213)	51,126 (3,135)	73,637 (4,871)	39,094 (2,261)	74,732 (3,667)
Refinement						
Resolution (Å)	29.42 – 2.30	29.77 – 2.20	29.76 – 2.06	29.86 – 1.80	29.95 – 2.24	29.69 – 1.80
R_{work}/ R_{free} (%)	16.4/18.5	17.4/20.7	17.7/20.0	18.4/20.5	18.4/21.1	17.0/18.9
No of atoms						
Protein	2,921	2,919	2,917	2,925	2,908	2,950
Lead	-	71	-	0	15	40
Other ligands[d]	44	15	57	2	18	39
Water	201	183	260	419	116	352

Average B-factors (Å^2)						
Protein	41.25	40.74	37.44	28.44	58.73	30.63
Lead	-	50.53	-	-	77.43	49.68
Ligand	62.84	54.77	55.82	46.11	72.00	52.17
Water	47.59	44.40	45.88	41.15	57.94	42.18
R.m.s deviations						
Bond lengths (Å)	0.007	0.007	0.007	0.007	0.007	0.007
Bond angles (°)	0.933	0.902	0.858	0.868	0.896	1.011
Ramachandran analysis						
Favored (%)	96.80	97.33	97.07	97.33	97.33	97.07
Allowed (%)	3.20	2.67	2.93	2.67	2.67	2.93
Outliers (%)	0.00	0.00	0.00	0.00	0.00	0.00
Clash score	4.56	3.55	2.02	2.40	3.08	2.34
PDB code	7MD1	7MD6	7MD8	7MD9	7MDA	7MDB

[a]The highest-resolution shell values are shown in parentheses.

[b-d]R_{merge}, R_{pim} and ligand details are given in the footnote to Table S4

Table S7. Minimal concentrations of selected bCSE inhibitors that have maximal potentiation of gentamycin *in vitro*.

Inhibitor / Strain	NL1 (μM)	NL2 (μM)	NL3 (μM)	Potentiation factor
S. aureus RN4220	30	20	5	≥ 3.5
S. aureus USA300	60	40	10	≥ 3.5
P. aeruginosa PA14	180	160	130	≥ 2
P. aeruginosa PA01	180	160	130	≥ 2

Table S8. Effect of H_2S-deficiency on *P. aeruginosa* PA14 transcriptome during the stationary phase of growth.

GO biological process	FC	P-value	FDR
alginic acid acetylation (GO:0051979)	28.24	7.30E-04	3.62E-02
alginic acid metabolic process (GO:0042120)	14.12	7.46E-07	6.11E-05
extracellular polysaccharide metabolic (GO:0046379)	14.12	2.89E-08	1.18E-05
extracellular polysaccharide biosynthetic (GO:0045226)	14.12	2.89E-08	9.46E-06
alginic acid biosynthetic process (GO:0042121)	12.1	3.85E-05	2.34E-03
response to oxygen levels (GO:0070482)	11.3	1.01E-03	4.62E-02
cellular response to oxygen levels (GO:0071453)	11.3	1.01E-03	4.49E-02
biofilm formation (GO:0042710)	6.33	5.98E-07	6.12E-05
multi-organism cellular process (GO:0044764)	6.18	2.81E-07	4.19E-05
monocarboxylic acid metabolic process (GO:0032787)	6.05	8.96E-04	4.19E-02
single-species biofilm formation (GO:0044010)	5.94	2.91E-06	2.08E-04
cellular polysaccharide metabolic (GO:0044264)	5.71	1.51E-08	2.47E-05
cellular carbohydrate metabolic process (GO:0044262)	5.71	1.51E-08	1.24E-05
polysaccharide metabolic process (GO:0005976)	5.65	1.76E-08	9.59E-06
polysaccharide biosynthetic process (GO:0000271)	5.19	3.12E-07	4.25E-05
cellular polysaccharide biosynthetic (GO:0033692)	5.19	3.12E-07	3.93E-05
cellular carbohydrate biosynthetic (GO:0034637)	5.19	3.12E-07	3.64E-05
drug metabolic process (GO:0017144)	5.17	4.35E-06	2.97E-04

Gene Ontology (GO) analysis (*99*) of differentially expressed genes in wt and *cse/cbs*(-) *P. aeruginosa* PA14 was performed using the gene ontology consortium online resource (geneontology.org). PANTHER overrepresentation test was run against GO database release of 2019-12-09 using Fisher test and default correction for FDR. Gene categories upregulated 5-fold or greater in wt as compared to *cse/cbs*(-) cells are listed.

Movie S1. Crystal structures of SaCSE in different states and bound to AOAA. The movie shows the X-ray crystal structure of SaCSE in tetrameric and monomeric states and compares the apo SaCSE structure (with PLP not bound to the enzyme covalently, green color) with the structure of the holoenzyme (cyan). In addition, the movie shows the AOAA-bound structure (light orange) superposed with the holoenzyme structure.

Movie S2. Putative druggable areas of SaCSE. The movie depicts druggable areas predicted *in silico* on the surface view of the tetramer, dimer, and monomer of SaCSE.

Movie S3. Structures of SaCSE bound to lead inhibitors. The movie shows crystal structures of SaCSE bound to NL1-NL3 inhibitors. The protein is in semi-transparent surface representation while inhibitors, Lys-PLP conjugate and adjacent residues are in sticks. The final scene shows superposed structures of the leads.

Movie S4. Rapid pyocyanin coloration of bCSE-deficient *P. aeruginosa* PA14 upon aeration. The overnight cultures of *P. aeruginosa* were left without aeration for 1 hour. Brief shaking caused rapid blue/green coloration of the bCSE-deficient (Δ) but not wt cells, that is indicative of the conversion of the transparent reduced form of pyocyanin to its oxidized blue form.

References and Notes

1. D. J. Payne, M. N. Gwynn, D. J. Holmes, D. L. Pompliano, Drugs for bad bugs: Confronting the challenges of antibacterial discovery. *Nat. Rev. Drug Discov.* **6**, 29–40 (2007). doi:10.1038/nrd2201 Medline

2. B. Ribeiro da Cunha, L. P. Fonseca, C. R. C. Calado, Antibiotic discovery: Where have we come from, where do we go? *Antibiotics* **8**, 45 (2019). doi:10.3390/antibiotics8020045 Medline

3. S. M. Schrader, J. Vaubourgeix, C. Nathan, Biology of antimicrobial resistance and approaches to combat it. *Sci. Transl. Med.* **12**, eaaz6992 (2020). doi:10.1126/scitranslmed.aaz6992 Medline

4. J. O'Neill, "Tackling drug-resistant infections globally: Final report and recommendations" (Wellcome Trust, 2016); https://wellcomecollection.org/works/thvwsuba.

5. A. Brauner, O. Fridman, O. Gefen, N. Q. Balaban, Distinguishing between resistance, tolerance and persistence to antibiotic treatment. *Nat. Rev. Microbiol.* **14**, 320–330 (2016). doi:10.1038/nrmicro.2016.34 Medline

6. N. Q. Balaban, S. Helaine, K. Lewis, M. Ackermann, B. Aldridge, D. I. Andersson, M. P. Brynildsen, D. Bumann, A. Camilli, J. J. Collins, C. Dehio, S. Fortune, J.-M. Ghigo, W.-D. Hardt, A. Harms, M. Heinemann, D. T. Hung, U. Jenal, B. R. Levin, J. Michiels, G. Storz, M.-W. Tan, T. Tenson, L. Van Melderen, A. Zinkernagel, Definitions and guidelines for research on antibiotic persistence. *Nat. Rev. Microbiol.* **17**, 441–448 (2019). doi:10.1038/s41579-019-0196-3 Medline

7. J. E. Michiels, B. Van den Bergh, N. Verstraeten, J. Michiels, Molecular mechanisms and clinical implications of bacterial persistence. *Drug Resist. Updat.* **29**, 76–89 (2016). doi:10.1016/j.drup.2016.10.002 Medline

8. J. W. Costerton, P. S. Stewart, E. P. Greenberg, Bacterial biofilms: A common cause of persistent infections. *Science* **284**, 1318–1322 (1999). doi:10.1126/science.284.5418.1318 Medline

9. A. E. Kirby, K. Garner, B. R. Levin, The relative contributions of physical structure and cell density to the antibiotic susceptibility of bacteria in biofilms. *Antimicrob. Agents Chemother.* **56**, 2967–2975 (2012). doi:10.1128/AAC.06480-11 Medline

10. H. R. Meredith, J. K. Srimani, A. J. Lee, A. J. Lopatkin, L. You, Collective antibiotic tolerance: Mechanisms, dynamics and intervention. *Nat. Chem. Biol.* **11**, 182–188 (2015). doi:10.1038/nchembio.1754 Medline

11. L. Dewachter, M. Fauvart, J. Michiels, Bacterial heterogeneity and antibiotic survival: Understanding and combatting persistence and heteroresistance. *Mol. Cell* **76**, 255–267 (2019). doi:10.1016/j.molcel.2019.09.028 Medline

12. A. Schulze, F. Mitterer, J. P. Pombo, S. Schild, Biofilms by bacterial human pathogens: Clinical relevance - development, composition and regulation - therapeutical strategies. *Microb. Cell* **8**, 28–56 (2021). doi:10.15698/mic2021.02.741 Medline

13. B. P. Conlon, *Staphylococcus aureus* chronic and relapsing infections: Evidence of a role for persister cells. *BioEssays* **36**, 991–996 (2014). doi:10.1002/bies.201400080 Medline

14. R. M. Donlan, J. W. Costerton, Biofilms: Survival mechanisms of clinically relevant microorganisms. *Clin. Microbiol. Rev.* **15**, 167–193 (2002). doi:10.1128/CMR.15.2.167-193.2002 Medline

15. L. R. Mulcahy, J. L. Burns, S. Lory, K. Lewis, Emergence of *Pseudomonas aeruginosa* strains producing high levels of persister cells in patients with cystic fibrosis. *J. Bacteriol.* **192**, 6191–6199 (2010). doi:10.1128/JB.01651-09 Medline

16. S. L. Percival, K. E. Hill, S. Malic, D. W. Thomas, D. W. Williams, Antimicrobial tolerance and the significance of persister cells in recalcitrant chronic wound biofilms. *Wound Repair Regen.* **19**, 1–9 (2011). doi:10.1111/j.1524-475X.2010.00651.x Medline

17. M. Huemer, S. Mairpady Shambat, J. Bergada-Pijuan, S. Söderholm, M. Boumasmoud, C. Vulin, A. Gómez-Mejia, M. Antelo Varela, V. Tripathi, S. Götschi, E. Marques Maggio, B. Hasse, S. D. Brugger, D. Bumann, R. A. Schuepbach, A. S. Zinkernagel, Molecular reprogramming and phenotype switching in *Staphylococcus aureus* lead to high antibiotic persistence and affect therapy success. *Proc. Natl. Acad. Sci. U.S.A.* **118**, e2014920118 (2021). doi:10.1073/pnas.2014920118 Medline

18. J. Davies, D. Davies, Origins and evolution of antibiotic resistance. *Microbiol. Mol. Biol. Rev.* **74**, 417–433 (2010). doi:10.1128/MMBR.00016-10 Medline

19. B. R. Levin, D. E. Rozen, Non-inherited antibiotic resistance. *Nat. Rev. Microbiol.* **4**, 556–562 (2006). doi:10.1038/nrmicro1445 Medline

20. J. Sebastian, S. Swaminath, R. R. Nair, K. Jakkala, A. Pradhan, P. Ajitkumar, De Novo emergence of genetically resistant mutants of *Mycobacterium tuberculosis* from the persistence phase cells formed against antituberculosis drugs *In vitro*. *Antimicrob. Agents Chemother.* **61**, e01343-16 (2017). doi:10.1128/AAC.01343-16 Medline

21. L. Luhachack, E. Nudler, Bacterial gasotransmitters: An innate defense against antibiotics. *Curr. Opin. Microbiol.* **21**, 13–17 (2014). doi:10.1016/j.mib.2014.06.017 Medline

22. H. Kimura, Signaling of hydrogen sulfide and polysulfides. *Antioxid. Redox Signal.* **22**, 347–349 (2015). doi:10.1089/ars.2014.6082 Medline

23. K. Shatalin, E. Shatalina, A. Mironov, E. Nudler, H_2S: a universal defense against antibiotics in bacteria. *Science* **334**, 986–990 (2011). doi:10.1126/science.1209855 Medline

24. C. Szabo, A timeline of hydrogen sulfide (H_2S) research: From environmental toxin to biological mediator. *Biochem. Pharmacol.* **149**, 5–19 (2018). doi:10.1016/j.bcp.2017.09.010 Medline

25. A. Mironov, T. Seregina, M. Nagornykh, L. G. Luhachack, N. Korolkova, L. E. Lopes, V. Kotova, G. Zavilgelsky, R. Shakulov, K. Shatalin, E. Nudler, Mechanism of H_2S-mediated protection against oxidative stress in *Escherichia coli*. *Proc. Natl. Acad. Sci. U.S.A.* **114**, 6022–6027 (2017). doi:10.1073/pnas.1703576114 Medline

26. L. Nzungize, M. K. Ali, X. Wang, X. Huang, W. Yang, X. Duan, S. Yan, C. Li, A. E. Abdalla, P. Jeyakkumar, J. Xie, *Mycobacterium tuberculosis metC* (Rv3340) derived

hydrogen sulphide conferring bacteria stress survival. *J. Drug Target.* **27**, 1004–1016 (2019). doi:10.1080/1061186X.2019.1579820 Medline

27. T. Toliver-Kinsky, W. Cui, G. Törö, S. J. Lee, K. Shatalin, E. Nudler, C. Szabo, H_2S, a bacterial defense mechanism against the host immune response. *Infect. Immun.* **87**, e00272-18 (2018). doi:10.1128/IAI.00272-18 Medline

28. M. Ren, B. Deng, X. Kong, K. Zhou, K. Liu, G. Xu, W. Lin, A TICT-based fluorescent probe for rapid and specific detection of hydrogen sulfide and its bio-imaging applications. *Chem. Commun.* **52**, 6415–6418 (2016). doi:10.1039/C6CC00966B Medline

29. X. Shen, G. K. Kolluru, S. Yuan, C. G. Kevil, Measurement of H_2S in vivo and in vitro by the monobromobimane method. *Methods Enzymol.* **554**, 31–45 (2015). doi:10.1016/bs.mie.2014.11.039 Medline

30. Q. Sun, R. Collins, S. Huang, L. Holmberg-Schiavone, G. S. Anand, C.-H. Tan, S. van-den-Berg, L.-W. Deng, P. K. Moore, T. Karlberg, J. Sivaraman, Structural basis for the inhibition mechanism of human cystathionine gamma-lyase, an enzyme responsible for the production of H_2S. *J. Biol. Chem.* **284**, 3076–3085 (2009). doi:10.1074/jbc.M805459200 Medline

31. D. Lee, S. Jeong, J. Ahn, N.-C. Ha, A.-R. Kwon, Crystal structure of bacterial cystathionine gamma γ-lyase in the cysteine biosynthesis pathway of *Staphylococcus aureus*. *Crystals* **9**, 656 (2019). doi:10.3390/cryst9120656

32. A. Asimakopoulou, P. Panopoulos, C. T. Chasapis, C. Coletta, Z. Zhou, G. Cirino, A. Giannis, C. Szabo, G. A. Spyroulias, A. Papapetropoulos, Selectivity of commonly used pharmacological inhibitors for cystathionine β synthase (CBS) and cystathionine γ lyase (CSE). *Br. J. Pharmacol.* **169**, 922–932 (2013). doi:10.1111/bph.12171 Medline

33. R. Wang, Physiological implications of hydrogen sulfide: A whiff exploration that blossomed. *Physiol. Rev.* **92**, 791–896 (2012). doi:10.1152/physrev.00017.2011 Medline

34. M. Whiteman, S. Le Trionnaire, M. Chopra, B. Fox, J. Whatmore, Emerging role of hydrogen sulfide in health and disease: Critical appraisal of biomarkers and pharmacological tools. *Clin. Sci.* **121**, 459–488 (2011). doi:10.1042/CS20110267 Medline

35. P. K. Yadav, V. Vitvitsky, H. Kim, A. White, U.-S. Cho, R. Banerjee, *S*-3-Carboxypropyl-l-cysteine specifically inhibits cystathionine γ-lyase-dependent hydrogen sulfide synthesis. *J. Biol. Chem.* **294**, 11011–11022 (2019). doi:10.1074/jbc.RA119.009047 Medline

36. T. Clausen, R. Huber, A. Messerschmidt, H. D. Pohlenz, B. Laber, Slow-binding inhibition of *Escherichia coli* cystathionine beta-lyase by L-aminoethoxyvinylglycine: A kinetic and X-ray study. *Biochemistry* **36**, 12633–12643 (1997). doi:10.1021/bi970630m Medline

37. J. Lowther, B. A. Yard, K. A. Johnson, L. G. Carter, V. T. Bhat, M. C. C. Raman, D. J. Clarke, B. Ramakers, S. A. McMahon, J. H. Naismith, D. J. Campopiano, Inhibition of the PLP-dependent enzyme serine palmitoyltransferase by cycloserine: Evidence for a novel decarboxylative mechanism of inactivation. *Mol. Biosyst.* **6**, 1682–1693 (2010). doi:10.1039/c003743e Medline

38. H. Mihara, T. Fujii, S. Kato, T. Kurihara, Y. Hata, N. Esaki, Structure of external aldimine of *Escherichia coli* CsdB, an IscS/NifS homolog: Implications for its specificity toward selenocysteine. *J. Biochem.* **131**, 679–685 (2002). doi:10.1093/oxfordjournals.jbchem.a003151 Medline

39. H. P. Ngo, N. M. F. S. A. Cerqueira, J.-K. Kim, M.-K. Hong, P. A. Fernandes, M. J. Ramos, L.-W. Kang, PLP undergoes conformational changes during the course of an enzymatic reaction. *Acta Crystallogr. D* **70**, 596–606 (2014). doi:10.1107/S1399004713031283 Medline

40. H. Y. Sagong, K. J. Kim, Structural Insights into substrate specificity of cystathionine γ-synthase from *Corynebacterium glutamicum*. *J. Agric. Food Chem.* **65**, 6002–6008 (2017). doi:10.1021/acs.jafc.7b02391 Medline

41. O. Trott, A. J. Olson, AutoDock Vina: Improving the speed and accuracy of docking with a new scoring function, efficient optimization, and multithreading. *J. Comput. Chem.* **31**, 455–461 (2010). Medline

42. C. Joce, J. A. Stahl, M. Shridhar, M. R. Hutchinson, L. R. Watkins, P. O. Fedichev, H. Yin, Application of a novel in silico high-throughput screen to identify selective inhibitors for protein-protein interactions. *Bioorg. Med. Chem. Lett.* **20**, 5411–5413 (2010). doi:10.1016/j.bmcl.2010.07.103 Medline

43. G. V. Smirnova, A. V. Tyulenev, K. V. Bezmaternykh, N. G. Muzyka, V. Y. Ushakov, O. N. Oktyabrsky, Cysteine homeostasis under inhibition of protein synthesis in *Escherichia coli* cells. *Amino Acids* **51**, 1577–1592 (2019). doi:10.1007/s00726-019-02795-2 Medline

44. K. Fesko, D. Suplatov, V. Švedas, Bioinformatic analysis of the fold type I PLP-dependent enzymes reveals determinants of reaction specificity in l-threonine aldolase from *Aeromonas jandaei*. *FEBS Open Bio* **8**, 1013–1028 (2018). doi:10.1002/2211-5463.12441 Medline

45. S. Huang, J. H. Chua, W. S. Yew, J. Sivaraman, P. K. Moore, C.-H. Tan, L.-W. Deng, Site-directed mutagenesis on human cystathionine-gamma-lyase reveals insights into the modulation of H_2S production. *J. Mol. Biol.* **396**, 708–718 (2010). doi:10.1016/j.jmb.2009.11.058 Medline

46. D. J. Dwyer, J. J. Collins, G. C. Walker, Unraveling the physiological complexities of antibiotic lethality. *Annu. Rev. Pharmacol. Toxicol.* **55**, 313–332 (2015). doi:10.1146/annurev-pharmtox-010814-124712 Medline

47. X. Zhao, Y. Hong, K. Drlica, Moving forward with reactive oxygen species involvement in antimicrobial lethality. *J. Antimicrob. Chemother.* **70**, 639–642 (2015). doi:10.1093/jac/dku463 Medline

48. B. W. Kwan, J. A. Valenta, M. J. Benedik, T. K. Wood, Arrested protein synthesis increases persister-like cell formation. *Antimicrob. Agents Chemother.* **57**, 1468–1473 (2013). doi:10.1128/AAC.02135-12 Medline

49. Y. Shan, A. Brown Gandt, S. E. Rowe, J. P. Deisinger, B. P. Conlon, K. Lewis, ATP-dependent persister formation in *Escherichia coli*. *mBio* **8**, e02267-16 (2017). doi:10.1128/mBio.02267-16 Medline

50. D. Wilmaerts, E. M. Windels, N. Verstraeten, J. Michiels, General mechanisms leading to persister formation and awakening. *Trends Genet.* **35**, 401–411 (2019). doi:10.1016/j.tig.2019.03.007 Medline

51. E. Forte, V. B. Borisov, M. Falabella, H. G. Colaço, M. Tinajero-Trejo, R. K. Poole, J. B. Vicente, P. Sarti, A. Giuffrè, The terminal oxidase cytochrome *bd* promotes sulfide-resistant bacterial respiration and growth. *Sci. Rep.* **6**, 23788 (2016). doi:10.1038/srep23788 Medline

52. L. E. Dietrich, A. Price-Whelan, A. Petersen, M. Whiteley, D. K. Newman, The phenazine pyocyanin is a terminal signalling factor in the quorum sensing network of *Pseudomonas aeruginosa*. *Mol. Microbiol.* **61**, 1308–1321 (2006). doi:10.1111/j.1365-2958.2006.05306.x Medline

53. G. W. Lau, D. J. Hassett, H. Ran, F. Kong, The role of pyocyanin in *Pseudomonas aeruginosa* infection. *Trends Mol. Med.* **10**, 599–606 (2004). doi:10.1016/j.molmed.2004.10.002 Medline

54. B. Rada, T. L. Leto, Pyocyanin effects on respiratory epithelium: Relevance in *Pseudomonas aeruginosa* airway infections. *Trends Microbiol.* **21**, 73–81 (2013). doi:10.1016/j.tim.2012.10.004 Medline

55. L. G. Rahme, E. J. Stevens, S. F. Wolfort, J. Shao, R. G. Tompkins, F. M. Ausubel, Common virulence factors for bacterial pathogenicity in plants and animals. *Science* **268**, 1899–1902 (1995). doi:10.1126/science.7604262 Medline

56. N. Möker, C. R. Dean, J. Tao, *Pseudomonas aeruginosa* increases formation of multidrug-tolerant persister cells in response to quorum-sensing signaling molecules. *J. Bacteriol.* **192**, 1946–1955 (2010). doi:10.1128/JB.01231-09 Medline

57. T. Das, S. K. Kutty, R. Tavallaie, A. I. Ibugo, J. Panchompoo, S. Sehar, L. Aldous, A. W. S. Yeung, S. R. Thomas, N. Kumar, J. J. Gooding, M. Manefield, Phenazine virulence factor binding to extracellular DNA is important for *Pseudomonas aeruginosa* biofilm formation. *Sci. Rep.* **5**, 8398 (2015). doi:10.1038/srep08398 Medline

58. L. E. Dietrich, T. K. Teal, A. Price-Whelan, D. K. Newman, Redox-active antibiotics control gene expression and community behavior in divergent bacteria. *Science* **321**, 1203–1206 (2008). doi:10.1126/science.1160619 Medline

59. B. J. C. Walsh, J. Wang, K. A. Edmonds, L. D. Palmer, Y. Zhang, J. C. Trinidad, E. P. Skaar, D. P. Giedroc, The response of *Acinetobacter baumannii* to hydrogen sulfide reveals two independent persulfide-sensing systems and a connection to biofilm regulation. *mBio* **11**, e01254-20 (2020). doi:10.1128/mBio.01254-20 Medline

60. N. Kaldalu, V. Hauryliuk, K. J. Turnbull, A. La Mensa, M. Putrinš, T. Tenson, *In Vitro* Studies of Persister Cells. *Microbiol. Mol. Biol. Rev.* **84**, e00070-20 (2020). doi:10.1128/MMBR.00070-20 Medline

61. A. Price-Whelan, L. E. Dietrich, D. K. Newman, Pyocyanin alters redox homeostasis and carbon flux through central metabolic pathways in *Pseudomonas aeruginosa* PA14. *J. Bacteriol.* **189**, 6372–6381 (2007). doi:10.1128/JB.00505-07 Medline

62. K. R. Allison, M. P. Brynildsen, J. J. Collins, Metabolite-enabled eradication of bacterial persisters by aminoglycosides. *Nature* **473**, 216–220 (2011). doi:10.1038/nature10069 Medline

63. P. O. Jensen, M. Givskov, T. Bjarnsholt, C. Moser, The immune system vs. *Pseudomonas aeruginosa* biofilms. *FEMS Immunol. Med. Microbiol.* **59**, 292–305 (2010). doi:10.1111/j.1574-695X.2010.00706.x Medline

64. T. F. Mah, G. A. O'Toole, Mechanisms of biofilm resistance to antimicrobial agents. *Trends Microbiol.* **9**, 34–39 (2001). doi:10.1016/S0966-842X(00)01913-2 Medline

65. P. S. Stewart, J. W. Costerton, Antibiotic resistance of bacteria in biofilms. *Lancet* **358**, 135–138 (2001). doi:10.1016/S0140-6736(01)05321-1 Medline

66. K. Shatalin, I. Gusarov, E. Avetissova, Y. Shatalina, L. E. McQuade, S. J. Lippard, E. Nudler, *Bacillus anthracis*-derived nitric oxide is essential for pathogen virulence and survival in macrophages. *Proc. Natl. Acad. Sci. U.S.A.* **105**, 1009–1013 (2008). doi:10.1073/pnas.0710950105 Medline

67. K. Y. Shatalin, A. A. Neyfakh, Efficient gene inactivation in *Bacillus anthracis*. *FEMS Microbiol. Lett.* **245**, 315–319 (2005). doi:10.1016/j.femsle.2005.03.029 Medline

68. R. P. Novick, S. Iordanescu, M. Surdeanu, I. Edelman, Transduction-related cointegrate formation between Staphylococcal plasmids: A new type of site-specific recombination. *Plasmid* **6**, 159–172 (1981). doi:10.1016/0147-619X(81)90064-0 Medline

69. M. Shen, H. Zhang, W. Shen, Z. Zou, S. Lu, G. Li, X. He, M. Agnello, W. Shi, F. Hu, S. Le, *Pseudomonas aeruginosa* MutL promotes large chromosomal deletions through non-homologous end joining to prevent bacteriophage predation. *Nucleic Acids Res.* **46**, 4505–4514 (2018). doi:10.1093/nar/gky160 Medline

70. B. Peng, W. Chen, C. Liu, E. W. Rosser, A. Pacheco, Y. Zhao, H. C. Aguilar, M. Xian, Fluorescent probes based on nucleophilic substitution-cyclization for hydrogen sulfide detection and bioimaging. *Chemistry* **20**, 1010–1016 (2014). doi:10.1002/chem.201303757 Medline

71. B. A. Forbes, D. F. Sahm, A. S. Weissfeld, *Bailey and Scott's Diagnostic Microbiology* (Mosby, ed. 10, 1998).

72. D. W. Essar, L. Eberly, A. Hadero, I. P. Crawford, Identification and characterization of genes for a second anthranilate synthase in *Pseudomonas aeruginosa*: Interchangeability of the two anthranilate synthases and evolutionary implications. *J. Bacteriol.* **172**, 884–900 (1990). doi:10.1128/JB.172.2.884-900.1990 Medline

73. F. Cockerill, "Method for dilution antimicrobial susceptibility test for bacteria that grow aerobically; approved standard—10th edition" (Clinical and Laboratory Standards Institute, 2015).

74. E. R. DeLeon, Y. Gao, E. Huang, M. Arif, N. Arora, A. Divietro, S. Patel, K. R. Olson, A case of mistaken identity: Are reactive oxygen species actually reactive sulfide species? *Am. J. Physiol. Regul. Integr. Comp. Physiol.* **310**, R549–R560 (2016). doi:10.1152/ajpregu.00455.2015 Medline

75. I. Keren, N. Kaldalu, A. Spoering, Y. Wang, K. Lewis, Persister cells and tolerance to antimicrobials. *FEMS Microbiol. Lett.* **230**, 13–18 (2004). doi:10.1016/S0378-1097(03)00856-5 Medline

76. J. H. Merritt, D. E. Kadouri, G. A. O'Toole, Growing and analyzing static biofilms. *Curr. Protoc. Microbiol.* **Chapter 1**, 1 (2005). Medline

77. P. Sabaeifard, A. Abdi-Ali, M. R. Soudi, R. Dinarvand, Optimization of tetrazolium salt assay for *Pseudomonas aeruginosa* biofilm using microtiter plate method. *J. Microbiol. Methods* **105**, 134–140 (2014). doi:10.1016/j.mimet.2014.07.024 Medline

78. E. F. Pettersen, T. D. Goddard, C. C. Huang, G. S. Couch, D. M. Greenblatt, E. C. Meng, T. E. Ferrin, UCSF Chimera—A visualization system for exploratory research and analysis. *J. Comput. Chem.* **25**, 1605–1612 (2004). doi:10.1002/jcc.20084 Medline

79. A. Borrel, L. Regad, H. Xhaard, M. Petitjean, A. C. Camproux, PockDrug: A model for predicting pocket druggability that overcomes pocket estimation uncertainties. *J. Chem. Inf. Model.* **55**, 882–895 (2015). doi:10.1021/ci5006004 Medline

80. V. Le Guilloux, P. Schmidtke, P. Tuffery, Fpocket: An open source platform for ligand pocket detection. *BMC Bioinformatics* **10**, 168 (2009). doi:10.1186/1471-2105-10-168 Medline

81. P. Schmidtke, V. Le Guilloux, J. Maupetit, P. Tufféry, fpocket: Online tools for protein ensemble pocket detection and tracking. *Nucleic Acids Res.* **38**, W582–W589 (2010). doi:10.1093/nar/gkq383 Medline

82. W. Li, A fast clustering algorithm for analyzing highly similar compounds of very large libraries. *J. Chem. Inf. Model.* **46**, 1919–1923 (2006). doi:10.1021/ci0600859 Medline

83. R. A. Jarvis, E. A. Patrick, Clustering using a similarity measure based on shared near neighbors. *IEEE Trans. Comput.* **C-22**, 1025–1034 (1973). doi:10.1109/T-C.1973.223640

84. J. Willett, *Similarity and Clustering in Chemical Information Systems* (Wiley, 1987).

85. N. M. O'Boyle, M. Banck, C. A. James, C. Morley, T. Vandermeersch, G. R. Hutchison, Open Babel: An open chemical toolbox. *J. Cheminform.* **3**, 33 (2011). doi:10.1186/1758-2946-3-33 Medline

86. W. Kabsch, XDS. *Acta Crystallogr. D* **66**, 125–132 (2010). doi:10.1107/S0907444909047337 Medline

87. P. D. Adams, P. V. Afonine, G. Bunkóczi, V. B. Chen, I. W. Davis, N. Echols, J. J. Headd, L.-W. Hung, G. J. Kapral, R. W. Grosse-Kunstleve, A. J. McCoy, N. W. Moriarty, R. Oeffner, R. J. Read, D. C. Richardson, J. S. Richardson, T. C. Terwilliger, P. H. Zwart, PHENIX: A comprehensive Python-based system for macromolecular structure solution. *Acta Crystallogr. D* **66**, 213–221 (2010). doi:10.1107/S0907444909052925 Medline

88. P. Emsley, B. Lohkamp, W. G. Scott, K. Cowtan, Features and development of Coot. *Acta Crystallogr. D* **66**, 486–501 (2010). doi:10.1107/S0907444910007493 Medline

89. D. Sehnal, R. Svobodová Vařeková, K. Berka, L. Pravda, V. Navrátilová, P. Banáš, C.-M. Ionescu, M. Otyepka, J. Koča, MOLE 2.0: Advanced approach for analysis of

biomacromolecular channels. *J. Cheminform.* **5**, 39 (2013). doi:10.1186/1758-2946-5-39 Medline

90. E. Krissinel, K. Henrick, Inference of macromolecular assemblies from crystalline state. *J. Mol. Biol.* **372**, 774–797 (2007). doi:10.1016/j.jmb.2007.05.022 Medline

91. S. Davis, P. D. Charles, L. He, P. Mowlds, B. M. Kessler, R. Fischer, Expanding proteome coverage with CHarge Ordered Parallel Ion aNalysis (CHOPIN) combined with broad specificity proteolysis. *J. Proteome Res.* **16**, 1288–1299 (2017). doi:10.1021/acs.jproteome.6b00915 Medline

92. S. Tyanova, T. Temu, J. Cox, The MaxQuant computational platform for mass spectrometry-based shotgun proteomics. *Nat. Protoc.* **11**, 2301–2319 (2016). doi:10.1038/nprot.2016.136 Medline

93. A. Bragonzi, Murine models of acute and chronic lung infection with cystic fibrosis pathogens. *Int. J. Med. Microbiol.* **300**, 584–593 (2010). doi:10.1016/j.ijmm.2010.08.012 Medline

94. C. Cigana, F. Bernardini, M. Facchini, B. Alcalá-Franco, C. Riva, I. De Fino, A. Rossi, S. Ranucci, P. Misson, E. Chevalier, M. Brodmann, M. Schmitt, A. Wach, G. E. Dale, D. Obrecht, A. Bragonzi, Efficacy of the novel antibiotic POL7001 in preclinical models of *Pseudomonas aeruginosa* pneumonia. *Antimicrob. Agents Chemother.* **60**, 4991–5000 (2016). doi:10.1128/AAC.00390-16 Medline

95. C. Cigana, S. Ranucci, A. Rossi, I. De Fino, M. Melessike, A. Bragonzi, Antibiotic efficacy varies based on the infection model and treatment regimen for *Pseudomonas aeruginosa*. *Eur. Respir. J.* **55**, 1802456 (2020). doi:10.1183/13993003.02456-2018 Medline

96. B. Langmead, S. L. Salzberg, Fast gapped-read alignment with Bowtie 2. *Nat. Methods* **9**, 357–359 (2012). doi:10.1038/nmeth.1923 Medline

97. S. Anders, P. T. Pyl, W. Huber, HTSeq—A Python framework to work with high-throughput sequencing data. *Bioinformatics* **31**, 166–169 (2015). doi:10.1093/bioinformatics/btu638 Medline

98. M. I. Love, W. Huber, S. Anders, Moderated estimation of fold change and dispersion for RNA-seq data with DESeq2. *Genome Biol.* **15**, 550 (2014). doi:10.1186/s13059-014-0550-8 Medline

99. M. Ashburner, C. A. Ball, J. A. Blake, D. Botstein, H. Butler, J. M. Cherry, A. P. Davis, K. Dolinski, S. S. Dwight, J. T. Eppig, M. A. Harris, D. P. Hill, L. Issel-Tarver, A. Kasarskis, S. Lewis, J. C. Matese, J. E. Richardson, M. Ringwald, G. M. Rubin, G. Sherlock; The Gene Ontology Consortium, Gene ontology: Tool for the unification of biology. *Nat. Genet.* **25**, 25–29 (2000). doi:10.1038/75556 Medline